Rheinisch-Westfälische Technische Hochschule Aachen
Fachrichtung Physik

Search for dark matter with scalar or pseudoscalar coupling in Run 2 data

BACHELORARBEIT
von Marcel Materok

zur Erlangung des ersten Hochschulgrades

Bachelor of Science (B.Sc.)

vorgelegt der
FAKULTÄT FÜR MATHEMATIK, INFORMATIK UND NATURWISSENSCHAFTEN
DER RWTH AACHEN

erstellt im
JANUAR 2016

angefertigt am
III. PHYSIKALISCHEN INSTITUT A

bei
PROF. DR. THOMAS HEBBEKER

Zweitgutachter
PROF. DR. CHRISTOPHER WIEBUSCH

Disclaimer:
This version contains minor corrections compared to the version handed in for evaluation.

Abstract

A sensitivity study for (pseudo)scalar coupling dark matter mediated by a scalar mediator in comparison with axial vector coupling dark matter mediated by a vector mediator has been performed. The analysis used data collected in 2015 with the CMS detector, at an LHC center-of mass energy of 13 TeV corresponding to an integrated luminosity of 41.9 pb^{-1}. No significant deviation of the transverse mass distribution of the electron and neutrino system from the Standard Model prediction has been found. Expected limits have been determined at a 95% confidence level for all used models and the sensitivity is compared using different kinematic selections. The so called W$'_{static}$ selection yields the lowest cross section limits for all models, when using high p$_T$-triggers. For low M$_{med}$, the signal from the axial vector model with ξ=-1 yields the lowest cross section limits, while for high M$_{med}$ signals of pseudoscalar or scalar dark matter yield the lowest cross section limits. For 1, 3 and 10 fb^{-1}of integrated luminosity expected limits are produced in order to provide an outlook for the sensitivity.

Kurzdarstellung

Eine Sensitivitätsstudie für (pseudo)skalar-koppelnde dunkle Materie mit einem skalaren Austauschteilchen im Vergleich mit axialvektor-koppelnder dunkler Materie übertragen von einem Vektormediator wurde durchgeführt. In dieser Analyse wurden Daten verwendet, die 2015 am CMS Detektor bei einer LHC-Schwerpunktsenergie von 13 TeV aufgenommen wurden und einer integrierten Luminosität von 41.9 pb^{-1} entsprechen. Keine signifikante Abweichung von der transversalen Massenverteilung des Elektron und Neutrino Systems von der Standard Model Erwartung wurde festgestellt. Die erwarteten Ausschlussgrenzen sind mit 95% Konfidenzniveau für alle genutzen Modelle bestimmt worden und die Sensitivität wurde mit verschiedenen kinematischen Selektionen verglichen. So genannte W$'_{static}$-Selektion liefern für alle Modelle die niedrigste Wechselwirkungsquerschnittausschlussgrenze, sofern hohe p$_T$-Trigger benutzt werden. Für niedrige M$_{med}$ liefert ein Signal im axialvektor Model mit ξ=-1 die niedristen Ausschlussgrenzen, während für hohe M$_{med}$ Signale mit pseudoskalarer oder skalarer dunkler Materie die niedrigste Ausschlussgrenzen liefern. Für die integrierte Luminositäten von 1, 3 and 10 fb^{-1} wurden Ausschlussgrenzen produziert, um einen Ausblick für die Sensitivität zu gewähren.

Table of Contents

Chapter 1

Introduction

In particle physics the most fundamental elements of matter are studied. Although its roots are in ancient Greece, where Leucippus together with Democritus are said to have developed a first rudimentary theory of atoms, particle physics is still an active field of research. Leucippus and Democritus thought of an atom to be indivisible, which is in greek 'ἄτομος', hence the name. But as of 1897, it was widely accepted, that atoms were divisible. This fact was proven by the discovery of the electron in 1897 by Sir Joseph John Thomson, for which he was awarded a Nobel Prize in 1906. Around this period of time, a lot of particles were discovered and concepts developed. This includes the photon (1895 by Wilhelm Röntgen), the nucleus of atoms (1908 to 1913, Geiger-Marsden experiment), positrons (1932, Carl D. Anderson) and electron neutrinos (1956, Cowan and Reines). One of the biggest developments regarding particle physics was the formulation of the Standard Model of particle physics, with its first version Sheden Glashow in 1961 and Steven Weinberg and Abdus Salam giving it its modern form in 1967.

However, the Standard Model is far from being a complete theory. One of its biggest problems is probably the most astounding revelation of the twentieth century in astrophysics: The understanding of the universe was changed by finding that baryonic matter, which is made up of protons and neutrons, makes up for only approximately 5 % of all matter. So called 'dark matter', which is not predicted by the Standard Model fills the universe, accounting for approximately one fifth of the universe and thus there is four to five times times more dark matter than ordinary matter. Although hints for this dark matter has been found in astrophysics, detecting this new type of matter proves to be a tough challenge.

To be able to understand dark matter completely several branches of physics have to cooperate. This includes theoretical physics, using general relativity and thermodynamics to describe how dark matter acts on large scales, astrophysics, providing evidence for its existence and insight into their interaction on astronomical scales, and particle physics, providing probable candidates and studying the interaction between dark matter and ordinary matter.

This thesis' purpose is to study whether scalar or pseudoscalar coupling dark matter is one of these probable candidates or if the 'traditional' approach of using vector or axial-vector coupling dark matter is a more suitable candidate in terms of sensitivity when searching at the Large Hadron Collider.

Chapter 2

Theoretical framework

2.1 Standard Model

If not indicated otherwise, this section is based on [1] and [2].
The Standard Model of Particle Physics (SM) was developed in the 1970s and subsequently the discoveries of the predicted W and Z bosons, the top quark, as well as the Higgs boson have given credibility to the SM. There are two different types of particles, fermions and boson, the difference being a half-integer spin in case of fermions and an integer spin in case of bosons. Different bosons transmitting the three fundamental forces, the electromagnetic force, the strong and weak nuclear force, have been found. While the electromagnetic force is transmitted via photons, the weak force is mediated by $W^{\pm}$ and Z^0 bosons. The strong force is transmitted by eight color charged gluons. The Higgs boson is different from the bosons mentioned before since it does not transmit a fundamental force and is responsible for the rest mass [3, 4].

However, not every particle is able to interact via all forces. Which force a particle couples to depends on its quantum numbers: To be able to couple to the electromagnetic force a particle has to have a non-zero electric charge and to be able to couple to the strong force, therefore a non-zero color charge. The weak nuclear force is able to couple to all elementary particles of the SM except for the gluons and the photon. For the fermions the boxes in figure 2.1 represent this behavior.

Unlike bosons, fermions are sorted in so called generations. There are three generations or families, with the most significant difference being the mass which increases with each generation. Every lepton generation consists of a charged lepton and an uncharged lepton-neutrino. Each lepton family has a quantum number, which is conserved. In contrast to leptons, quarks have a color charge. There are three different color charges, red, green and blue and their anticolor. Quarks can only be observed in bound states which implies that only colorless combinations of elementary particles are able to move freely. The most common colorless particles are baryons, consisting of three quarks like protons or neutrons, and mesons, which are quark anti-quark pairs, for example the pions $\pi^{\pm}$ and π^0, however, at LHCb pentaquark states may have been found [5]. All known elementary particles of the SM are shown in figure 2.1 below.

Even though the SM is precise and predicts a variety of phenomenons well, there are quite a number of findings, the SM is not yet able to describe. Examples include, for example to gravity, the predominance of matter over antimatter in the universe or the astrophysically observed dark matter. Thus theories beyond the SM are needed.
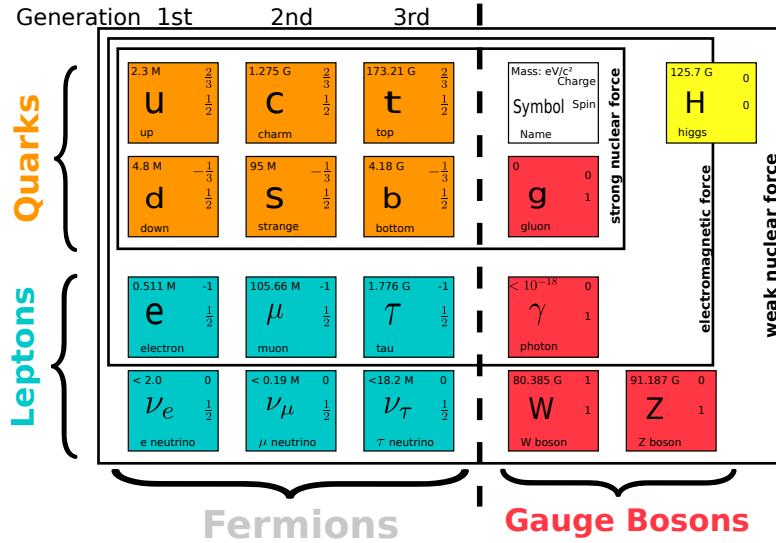
Figure 2.1: Standard Model of Particle Physics, values taken from [6].
The boxes in this figure show the coupling of the three generations of both types of fermions to the mediators of the three fundamental forces of the SM.

2.2 Dark matter

Dark matter is of special interest in particle physics due to astrophysical evidence but no particle physics evidence of dark matter having been found. For example, experiments measuring the extended rotation curve of distant galaxies such as M33, as done in [7], show unexpected behavior, assuming one can observe all matter and gravitationally interacting objects, namely the outer most parts of M33 are faster than expected. Figure 2.2 illustrates that a rather big contribution of gravitational force in the outer part of the galaxy is presumably due to dark matter halo.
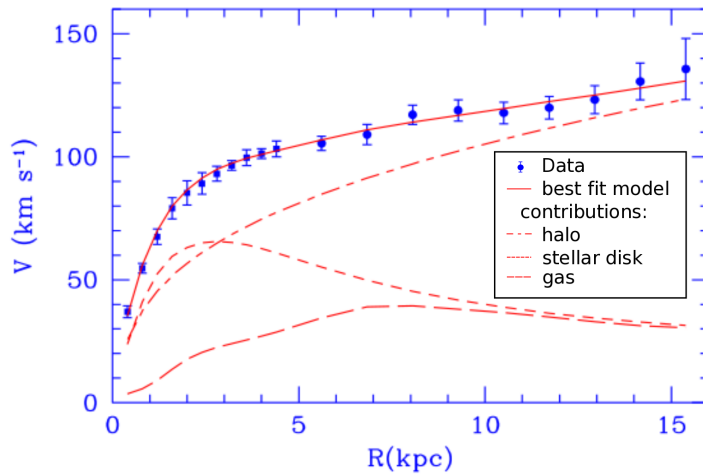

Figure 2.2: The M33 rotation curve with dark matter contributions to the best fit model is shown; adapted from [7].

This can also be explained using the 'Modified Newtonian Dynamics' (MOND) [8] approach, however, this approach cannot explain various effects and measurements, as described in the first part of [9], which indicate the existence of dark matter. Such examples are given by the measurements of the Wilkinson Microwave Anisotropy Probe (WMAP) [10] and Planck spacecraft [11], whose data taken can be explained well using the 'ΛCDM' Model [12].

One of the strongest evidence found so far is gravitational lensing [13–15]. This phenomenon is often split into two categories, strong and weak. While strong gravitational lensing can be used to probe the central mass distribution of cluster cores by studying so called giant arcs, weak gravitation lensing can be used to probe mass distributions in clusters. Due to requirements on the mass density of a cluster core, strong lensing is used less than weak lensing. Owing to the fact that galaxies are not necessarily intrinsically symmetric, weak lensing depends on a statistical approach by averaging over many images. Both types of lensing are sensitive only to the surface mass density projected along the line-of-sight, irrespective of its composition or physical state [16]. Due to this fact, the dark matter potential has been mapped using weak shear [17].

Even though astrophysical evidence for dark matter has been found using a variety of different approaches, evidence on particle level has yet to be found. To find new evidence, there are three different approaches, namely direct and indirect detection and the production at colliders. These methods are visualized in figure 2.3.
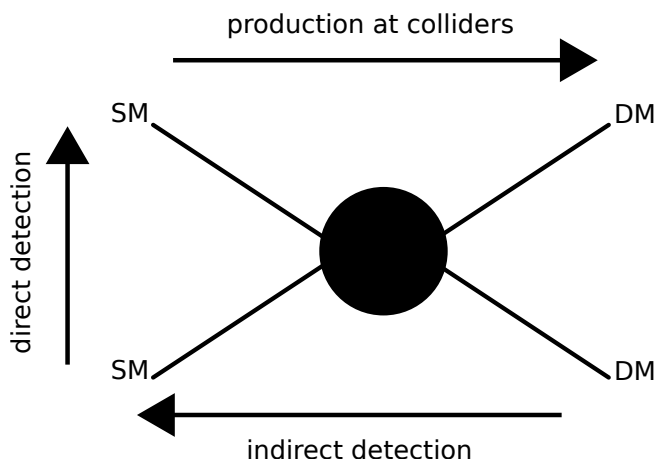

Figure 2.3: The three dark matter search methods are shown: direct, indirect and collider searches; the arrow indicates the arrow of time.

In contrast to experiments like XENON100 [18] and LUX [19], in which the principle of direct detection is used, by measuring the scattering of SM matter and dark matter, experiments like IceCube [20] and AMS [21, 22] attempt to detect dark matter indirectly, mainly by observing excess of SM matter. However, this analysis focuses on the production of dark matter at a collider, the Large Hadron Collider. Detection of data is achieved with the Compact Muon Solenoid detector, which is explained in more detail in chapter 3.

Possible candidates for dark matter have to fulfill certain criteria to be considered a good candidate [23]: The dark matter candidate has to match the appropriate relic density, be consistent with Big Bang Nucleosynthesis [24] and allow stellar evolution. In order to be consistent with limits already set, astrophysical bounds [10, 11, 21, 22], gamma-ray constraints [25], constraints on self-interactions [26] and limits from direct DM searches [18, 19] have to

be fulfilled. Additionally, any candidate has to be cold, electrically neutral and be able to be probed experimentally.

One type of candidate particles that fulfills this list reasonably well is the class of **W**eakly **I**nteracting **M**assive **P**articles, so called WIMPs. By construction, WIMPs are electrically neutral, thus not interacting via the electromagnetic force and not being able to be observed by optical telescopes. The interaction strength of a WIMP has to be in the same order of magnitude as the weak interaction.

Due to these facts, the dark matter candidate used in this thesis is a WIMP. From an experimentalist point of view, it is most important, that WIMPs only interact gravitationally thus leave the detector unseen. Thus any search for dark matter at a collider has to be produced along other particles which are detectable.The search signature of this analysis is the mono-lepton channel, which is subsequently discussed.

2.3 Model

Until now mainly vector boson mediated dark matter coupling spin independently (vector (V)) or spin dependently (axial-vector (AV)) has been considered [27]. However due to the recent discovery of a Higgs-like boson [28, 29], a scalar elementary particle, the search for dark matter with scalar (S) or pseudoscalar (PS) coupling has been a topic of interest [30–32]. One interesting questions is whether pseudoscalar or axial-vector coupling dark matter is more sensitive for searches at CMS. As Dennis Noll's bachelor's thesis [33] has shown, the PS model has more events at high M_T than the AV ξ=+1 model, see figure 2.4, which indicates a better sensitivity.
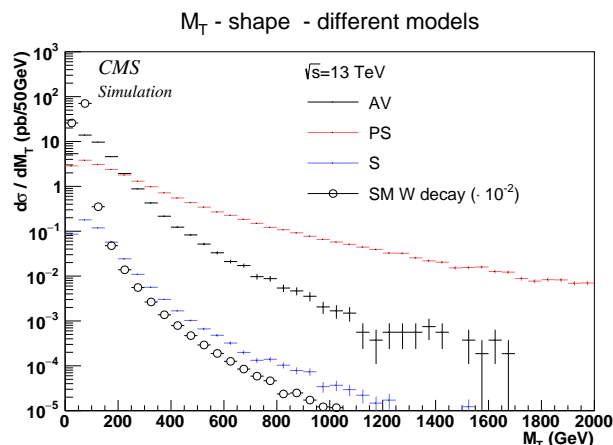
Figure 2.4: Comparison of cross section for different couplings and decays, plot made by Dennis Noll [33].

As seen in figure 2.4, the pseudoscalar model provides higher differential cross sections than the scalar model. The higher cross section in the PS case can be explained with the respective Lagrangians $\mathcal{L}_{(P)S}$ [34]:

$$\mathcal{L}_S \supset -\frac{1}{2}M_{med}^2 S^2 - g_{DM}S\bar{\chi}\chi$$

$$\mathcal{L}_{PS} \supset -\frac{1}{2}M_{med}^2 P^2 - g_{DM}P\bar{\chi}\gamma^5\chi$$

5

The difference between these Lagrangians is the extra γ^5 term in $\mathcal{L}_{PS}$. This term introduces a spin sensitivity to the pseudoscalar case, which causes the higher cross section. Similarly, this can be observed in the comparison of vector and axial-vector models [34].

In contrast to the (P)S models, the (A)V models an additional parameter [35], includes the interference parameter and is often denoted as ξ. This parameter can be defined as $\xi = \frac{g_d}{g_u}$ [27], with g_d and g_u being the couplings to the down and up quarks respectively. Constructive interference can be observed in case of ξ=-1, leading to higher process cross sections. For ξ=+1 destructive interference can be observed, leading in turn to lower process cross sections. Taking into account that the parameter ξ is restricted to $\xi \approx 1$ for effective field theory approaches [36], the range of ξ being able to be used in simplified models is not yet resolved and still under investigation [37].

To be able to determine, which coupling (A)V or (P)S, is most sensitive, a comparable channel has to be used. Taking into account that (P)S couplings are different to (A)V, a channel with the same final state and related means of production has to be chosen. As the Mono-W channel is studied in the Aachen workgroup for (A)V coupling, a Mono-W channel for (P)S coupling dark matter is chosen. Additionally, this channel has been proposed in talks at CMS [38].

Owing to the fact, that the only known elementary scalar boson so far, is the Higgs boson, and the Higgs boson is able to be produced in the Mono-W channel [39,40], the Mono-W channel is utilized for this thesis. In the case of the Higgs boson, this channel often is called associated production of the Higgs, utilizing the so called Higgsstrahlung mechanism [41]. However, this thesis is not investigating Higgs physics, especially the invisible Higgs decay, thus a mediator, that generally behaves like the SM Higgs, but does not necessarily have to be the found SM Higgs, is used. Therefore a process related to associated production is used. The mediator is radiated from an excited W boson and decays into a pair of dark matter.

Both sets of models, (P)S, figure 2.5a, and (A)V, shown in figure 2.5b, are produced in a channel, with the final state consisting of a pair of dark matter particles, one neutrino and one lepton as proposed in [35]. Due to neutrinos as well as dark matter not being able to be detected, these particles are combined as missing transverse energy E_T^{miss}. The lepton, however, can be measured well, thus channel of production is considered to be a mono-lepton channel. This analysis is limited to electrons and positrons as the lepton and in addition, the mediator for each model is required to decay into dark matter particles, as the mediator possibly decaying into other particles only changes the branching ratio.

Owing to the facts that this analysis is aiming to be a sensitivity study, three masses were simulated in private production. These masses have been chosen based on a shape analysis on generator level. The mediator masses are selected at points at which the shape changes significantly [42].

Figure 2.6 shows the production cross section for the three selected mass points of M_{med}=50, 500 and 2000 GeV for the four used models. The production cross section of the AV ξ=$\pm$1 models are abbreviated $\sigma_{prod}\,\xi = \pm 1$ and the production cross section of the (P)S models are abbreviated σ_{prod}(P)S. The (P)S models features a strong M_{med} dependence, which can be explain using the Feynman diagram in figure 2.5a. As a result of the fact, that the mediator has to be radiated by an exited W boson, this W boson is required to be off-shell. As the mediator mass increases, the W boson has to be further off-shell. This is increasingly improbable and thus the production cross section decreases.

(a) Feynman diagram for the (pseudo)scalar model

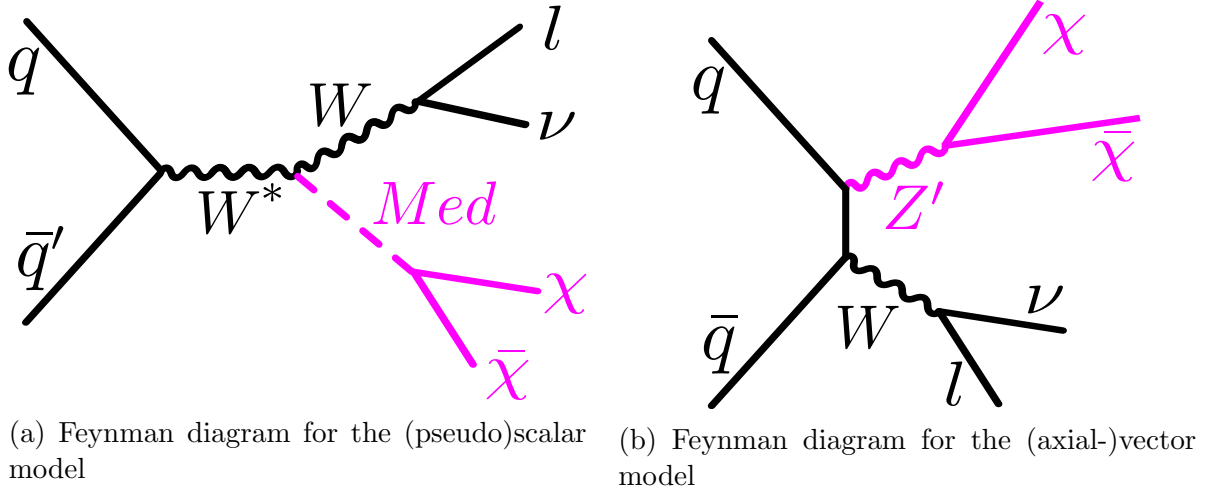(b) Feynman diagram for the (axial-)vector model

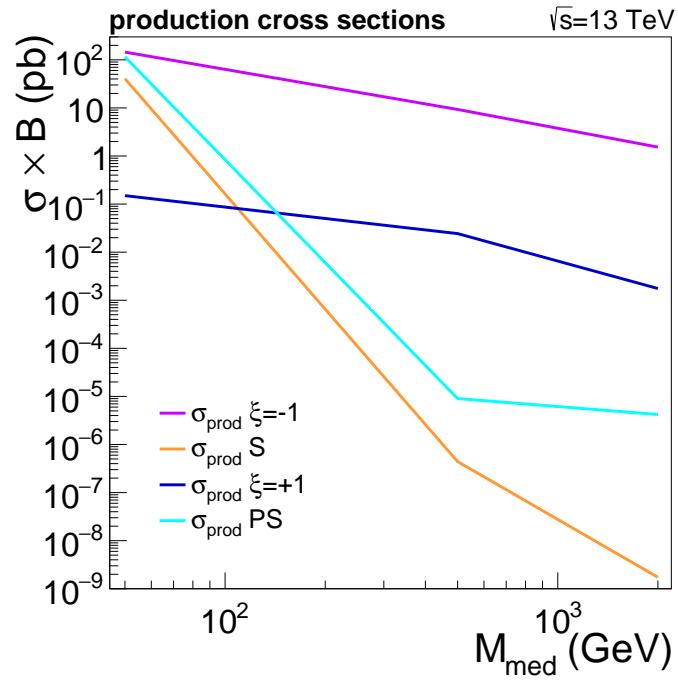Figure 2.5: Feynman diagrams for both sets of models are shown.

Figure 2.6: The production cross section of an AV ξ=-1 (violet), AV ξ=1 (blue), PS (cyan) and S (orange) signal with m_χ=10 GeV is shown as a function of M_{med}.

Chapter 3

CMS Detector

The Compact Muon Solenoid (CMS) detector is a general-purpose detector, that operates at the Large Hadron Collider (LHC) at the European Organization for Nuclear Research (CERN) and is located underground near Geneva. CERN operates four large detectors that records collisions of the LHC. These are split into two groups. One of which is the group of detectors, that are dedicated to a single purpose. This group consists of LHCb [43], which investigates bottom and bottom anti-quark physics, and ALICE [44], which studies strongly interacting matter at extreme energy densities. The other group contains the ATLAS [45] and CMS general-purpose detectors [46], aiming to study a wide range of particle physics.

The CMS utilizes four different types of detectors and a superconducting solenoid, that is able to produce a magnetic field of up to 3.8 T. Starting from the center to the outside, the detectors are installed in the following order, as seen in figure 3.1:

- Silicon pixels and strip detectors: the silicon trackers, with the pixel detectors being the inner most detectors. The tracking system is used to accurately measure the momenta of charged particles.

- Electromagnetic Calorimeter (ECAL): scintillating $PbWO_4$ crystals to measure the total energy of electrons and photons with high resolution.

- Hadronic Calorimeter (HCAL): build out of brass and plastic scintillators to measure the total energy of hadrons and to prevent most particles from escaping.

- Muon Chambers: consist of drift tubes and resistive plate chambers in the barrel and cathode strip detectors and resistive plate chambers in the endcaps and is used to detect and measure muons.

The detector has different regions, the forward region, the barrel and endcap. These parts can be differentiated by the pseudorapidity η, which is defined as

$$\eta = -\ln(\tan(\frac{\theta}{2})) \approx \frac{1}{2}\ln(\frac{|\vec{p}| + p_L}{|\vec{p}| - p_L}),$$

θ being the polar angle used in polar coordinates. The region with $|\eta| < 1.4$ is denoted barrel, for $1.4 < |\eta| < 3$ the region is denoted endcap and the region in which $3 < |\eta| < 5$ is true, is the very forward region. The hadron forward detector is located in the forward region.

The measurable quantities which are integral to this analysis, are the transverse energy $\vec{E}_T$, which is defined as $\vec{E}_T = \vec{E} \cdot sin(\theta)$, the transverse momentum $\vec{p}_T$, which is defined as $\vec{p}_T = \vec{p} \cdot sin(\theta)$ and the missing transverse energy $\vec{E}_T^{miss} = -\sum \vec{p}_T$. The angle between $\vec{p}_T$ and $\vec{E}_T^{miss}$ is denoted as $\Delta\phi$, and can be used to define the transverse mass M_T as $\sqrt{2\vec{p}_T\vec{E}_T^{miss} \cdot (1 - cos(\Delta\phi))}$.
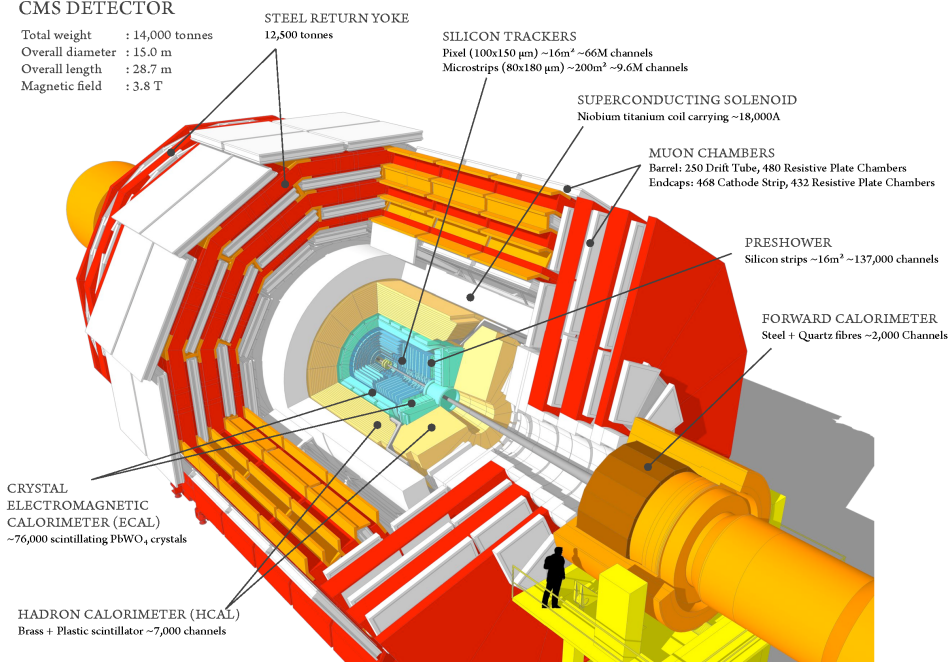

Figure 3.1: A schematic overview of CMS, taken from [47],is given.

More detailed information regarding the CMS detector can be found here: [46]

3.1 Run 2 Data

This analysis is based in part on data taken with the CMS. The data set is based on run 2015 B with a magnetic field of 3.8 T with 50 ns bunch spacing. Only certified runs which amount to approximately 41.9 pb^{-1} of integrated luminosity are used. Due to the fact, that the LHC had a rise in center of mass energy to $\sqrt{s}$=13 TeV after the first long shutdown. The detector was not yet fully calibrated and several triggers, such as the low p$_T$ electron trigger, are not yet well understood. As a direct result throughout the majority of this analysis, high p$_T$ electron triggers are used.

Chapter 4

Signal generation and computational setup

Most commonly used generators do not yet include models for the (P)S signals. The JHU generator is a relatively new tool that is able to generate scalar mediators in simplified models with either S or PS coupling [48–50]. This generator has been proposed as a tool for the investigated (P)S models in CMS "MC & Interpretation" meetings [51, 52]. Therefore the JHU generator has been used to generate (P)S signals, while MadGraph [53] has been used for the AV signals.

However, the decay to dark matter is not yet implemented in this generator. Chiaran Williams developed a tool called boltdmdec which is able to decay the mediator into dark matter particles. Details regarding the scaling of the cross section can be found in [33].

The runs generated with $2 \cdot 10^5$ events for a width Γ of $\frac{M_{med}}{8\pi}$ and mediator masses of M_{med} = 50 GeV, 500 GeV and 2000 GeV. These masses have been selected to cover a large phase space of the model at points with significant changes in the M_T shape [42]. The dark matter mass m_χ is fixed to 10 GeV. As Dennis Noll's thesis [33] has shown, the mediator couplings g_W and g_{DM} only have an impact on the production cross section, however, not on the shape. For simplicity, these coupling values have therefore been set to 1.

In order to be able to use these samples as a signal detectable in CMS, hadronization with Pythia 8 [54] and a full detector simulation utilizing the CMSSW framework [55] have to be performed.

The simulated signals are compared to AV signals with $\xi=\pm1$. These signals were produced for previous analyses of the Aachen work group for the same set of M_{med} and the dark matter mass m_χ is fixed to 10 GeV, with the exception of $\xi=1$ and $M_{med} = 2000$ GeV. This sample was missing and as a replacement a sample with m_χ is 100 GeV from the official production was used. All of these samples are produced with approximately $3 \cdot 10^4$ events after jet matching, with the exception of the sample for $\xi=1$ and $M_{med} = 2000$ GeV, which has approximately 10^5 events.

The simulated signals can be analysed together with data taken in CMS and backgrounds generated with Monte Carlo generators such as Pythia [54] and Powheg [56] in the TAPAS [57] framework. The TAPAS framework is also used to produce most of the plots.

Chapter 5

Kinematic selection

5.1 Electron and Missing Transverse Energy Selection

The event selection follows the 8 TeV lepton and missing transverse energy analysis [27] as it is very similar.

As described in section 2.3 an event signature with a single high p_T electron is expected in the studied models, along with three or more particles that cannot be detected directly, dark matter and neutrinos, thus leading to experimentally observed missing energy E_T^{miss}. This missing energy is reconstructed utilizing the particle-flow technique [58–62]. The particle-flow event algorithm reconstructs and identifies each individual particle by combining information from various elements of the CMS detector. The energy of the electrons is determined by combining three measurements: The tracker measures the electron momentum at the primary interaction vertex, the corresponding ECAL cluster measures the energy of the electron and the sum of the energies of photons that are compatible with originating from bremsstrahlung along the electron track is measured. For this analysis, particle flow missing transverse energy, pfMET is used [63] and is preliminarily corrected for jet energy calibration [64, 65] and their propagation to the E_T^{miss} (type-1 corrections).

To select a candidate event an electron has to fulfill the high energy electron pair identification v6 [66], see table A.1. The electron also has to be triggered by either the *HLT_Ele27_eta2p1_WPLoose_Gsf* or *HLT_Ele105_CaloIdVT_GsfTrkIdT* trigger. If the selected electron is triggered by the *HLT_Ele27_eta2p1_WPLoose_Gsf* trigger, it has a p_T of at least 27 GeV. Additional an offline cut of $p_T > 35$ GeV is applied as this trigger has a efficiency plateau above a p_T of 35 GeV. Despite the fact that the detector effects are not yet sufficiently well understood for the low p_T region, the selection will be optimized in section 5.3 utilizing this trigger. Nevertheless the optimization is tested for future results. However, analyzing the data taken requires a well understood trigger. For this purpose the *HLT_Ele105_CaloIdVT_GsfTrkIdT* trigger is used. It requires a p_T of at least 105 GeV und the trigger is fully efficient for a p_T which is larger than 120 GeV, as shown in [67, 68], thus an additional offline cut is applied. This trigger is used to lessen the influence of the W induced background and of the low p_T region.

Electrons are reconstructed as electromagnetic calorimeter clusters that can be matched to a tracker track. Additionally they have to be within the acceptance region of the barrel, $|\eta| < 1.442$, or the endcaps, $1.56 < |\eta| < 2.5$. This criterion ensures that no electron in the transition region, in which the misidentification is the most probable, is accepted. The electron

also has to have an electron-like shape and must be sufficiently isolated, which means that all tracks in the proximity of the candidate originate from the same primary vertex and have a sum of p$_T$ of less than 5 GeV within a cone of ΔR = $\sqrt{\Delta\phi^2 + \Delta\eta^2}$=0.3.

5.2   Backgrounds

There are several processes whose final state is similar to that of the signal. These processes are listed in table 5.1.

The backgrounds can be estimated from simulation either at leading order (LO) or next-to leading order (NLO). The dominant process is the decay of a W $\rightarrow$ $l\nu$. This process is irreducible due to the topology of this process being almost identical to that of the signal. Even though the W Boson off-shell samples are produced at LO, a K-factor was computed by members of the Aachen W'-group. The K-factor corrects the LO cross section for electro-weak effects at NLO and QCD effects at NNLO [69].

Other processes are Drell-Yan (DY), where one of the leptons is either lost or out of the acceptance, $t\bar{t}$ in the semileptonic or dileptonic decay channel and diboson decays, where all but one lepton escape detection. Of the diboson decays, the WZ decay contributes the most, with the W boson decaying to a lepton and a neutrino and the Z boson decaying into a pair of neutrinos. The background with the largest cross section is QCD multijet, even though it is efficiently rejected with the selection criteria. Due to the fact that simulations of the QCD mulitjet process are sensitive to how many corrections on the leading order are produced, this process is derived from data. The data driven method used is the ABCD-Method, see figure 5.1, and was used in previous lepton and missing transverse energy analyses in CMS, for example in [70, 71]. In this method a signal region, 0.4 <p$_T$/E_T^{miss}< 1.5, and a QCD region, p$_T$/E_T^{miss}>1.5, are defined. In both the signal and the QCD region two extra regions, one with non isolated and one with isolated leptons are defined and named A and B for the signal region and C and D for the QCD region, respectively. Region A is then used to obtain a QCD template sample. Then the regions C and D are used to determine the normalization of the fake rate, which then is applied to region A to obtain region B.

Owing to the fact, that the data taken is fixed to a certain amount of integrated luminosity $\mathcal{L}_{int}$, while the simulated expectation is not, the total number of simulated events N$_{MC}$ has to be weighted with a factor f which is defined as

$$f = \frac{\sigma\mathcal{L}_{int}}{N_{MC}}$$

with σ being the cross section of the process.

Table 5.1: A list of backgrounds with their generators used for simulation and their cross sections at leading order (LO) or next-to leading order (NLO). The masses are given in GeV.

|	Background	Generator		σ (pb)
W on-shell	W$\to$ lν M $<$ 200 GeV	MC@NLO	NLO	61526.7
W off-shell	W$\to$ eν M $\in$ (200,500) GeV	Pythia 8	LO	6.095
	W$\to$ eν M $\in$ (500,1000) GeV	Pythia 8	LO	0.201
	W$\to$ eν M $\in$ (1000,3000) GeV	Pythia 8	LO	0.0141
	W$\to$ eν M $>$ 3000 GeV	Pythia 8	LO	3.23e-05
	W$\to$ $\mu\nu$ M $\in$ (200,500) GeV	Pythia 8	LO	6.095
	W$\to$ $\mu\nu$ M $\in$ (500,1000) GeV	Pythia 8	LO	0.201
	W$\to$ $\mu\nu$ M $\in$ (1000,3000) GeV	Pythia 8	LO	0.0141
	W$\to$ $\mu\nu$ M $>$ 3000 GeV	Pythia 8	LO	3.23e-05
	W$\to$ $\tau\nu$ M $\in$ (200,500) GeV	Pythia 8	LO	6.095
	W$\to$ $\tau\nu$ M $\in$ (500,1000) GeV	Pythia 8	LO	0.0201
	W$\to$ $\tau\nu$ M $\in$ (1000,3000) GeV	Pythia 8	LO	0.0141
	W$\to$ $\tau\nu$ M $>$ 3000 GeV	Pythia 8	LO	3.23e-05
Drell-Yan	Z/$\gamma \to ll$ M$_{ll}$ $\in$ (10,50) GeV	MC@NLO	NLO	18610
	Z/$\gamma \to ll$ M$_{ll}$ $>$ 50 GeV	MC@NLO	NLO	6104
t$\bar{\text{t}}$	t$\bar{\text{t}}$ M$_{\text{t}\bar{\text{t}}}$ $<$ 700 GeV	PowHeg	NLO	730
	t$\bar{\text{t}}$ M$_{\text{t}\bar{\text{t}}}$ $\in$ (700,1000) GeV	PowHeg	NLO	67.233
	t$\bar{\text{t}}$ M$_{\text{t}\bar{\text{t}}}$ $\in$ (1000,∞) GeV	PowHeg	NLO	18.0602
Diboson	WW	Pythia 8	LO	63.21
	WZ	Pythia 8	LO	22.82
	ZZ	Pythia 8	LO	10.32
QCD	Multijet	derived from data		
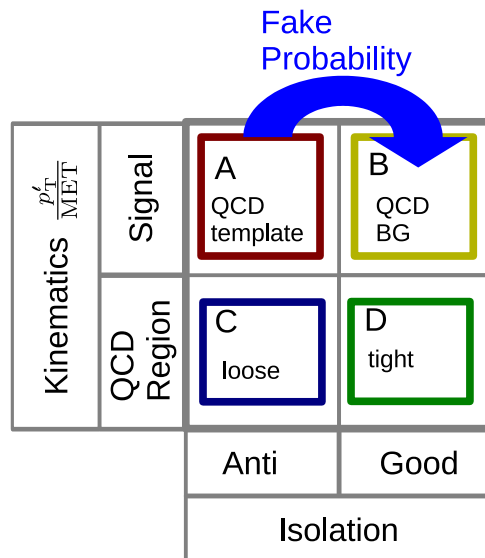
Figure 5.1: Shown is the ABCD method, taken from [70]. In region A a QCD template sample is obtained, with regions C and D are used to termine the normalization. Region B is the signal region. These regions are distinguished by p$_T$/E_T^{miss}.

5.3 Optimization of the Selection

5.3.1 Motivation

In figure 5.2 the major backgrounds and a signal for each model. In this plot no selection and low p_T triggers are applied. While the backgrounds are stacked, the signals are presented independently.
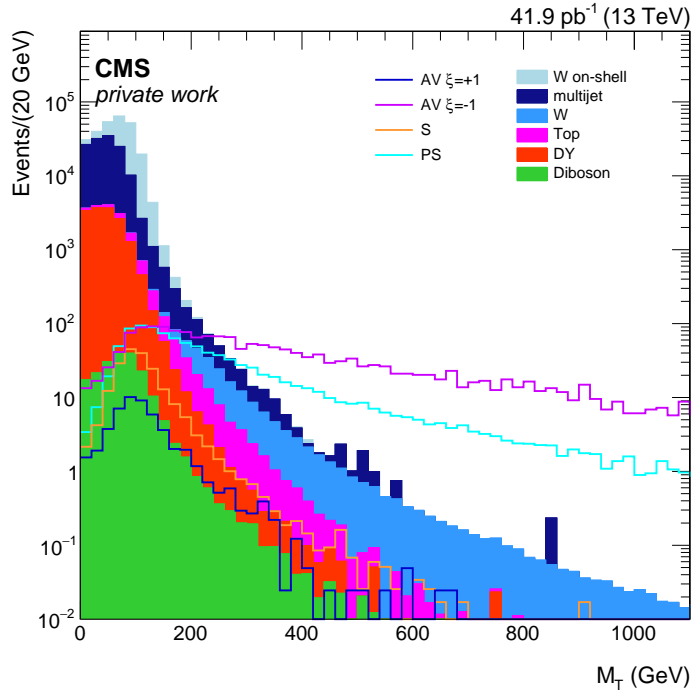

Figure 5.2: M_T distribution of backgrounds and signals with no signal selection and low p_T triggers applied. The signals are produced with M_{med}=50 GeV.

The background peaks around M_T=80 GeV, while the signal peaks around 130 GeV in M_T. This can be understood considering that the most significant background is induced by W boson decay of transverse mass $M_T \approx 80$ GeV, for the signals, however, at this transverse mass, a mediator is unlikely to be produced yet and additional energy, thus higher M_T is required. If an analysis was performed at this stage the data would be dominated by background and the sensitivity to the signal would be low. In order to increase the sensitivity, the signal to background ratio has to be improved by reducing the background contribution. This can be achieved by selecting events using the variables $\Delta\phi(e,E_T^{miss})$ and p_T/E_T^{miss}, as these spectra have regions in which there is little signal and a big amount of background, as seen in figure 5.3. All four studied models are approximately constant for $\Delta\phi(e,E_T^{miss})$ <1.4, but have a more steep slope than all background processes with the exception of the W boson induced background. The signals and the W background peak around $\Delta\phi(e,E_T^{miss})=\pi$ due to the back-to-back topology of the decays. In p_T/E_T^{miss}, the number of signal events decreases faster than any background and peaks for $p_T/E_T^{miss}\approx1$.

14

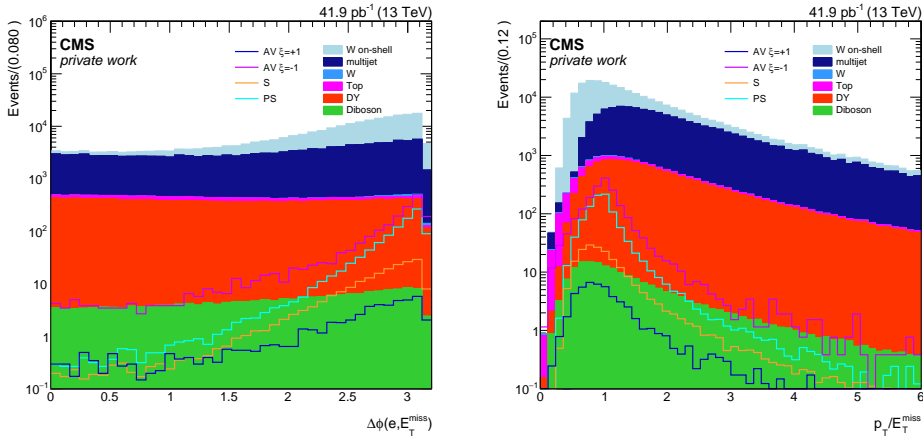Figure 5.3: On the left before any selection but low p_T triggers are $\Delta\phi(lep, E_T^{miss})$, on the left, and p_T/E_T^{miss}, on the right; regions with low signal contributions can be found. The signals are produced with M_{med}=50 GeV.

5.3.2 Method and Result

There are generally two distinct approaches to selecting on a variable, the first one being a static selection, which means that the selection does not change. This approach has been used in beyond the SM searches before, for example [27]. The alternative is a varying selection. As mono-lepton searches usually are performed in the M_T distribution, a M_T dependent selection is optimized for this work in the following way:

The M_T spectrum and the distribution of the selection variables are binned, and for each M_T bin the following process is performed:
For each bin in the distribution the signal efficiency and significance s is computed

$$ s = \frac{N_{sg}}{\sqrt{N_{sg} + N_{bg}}} $$

for N_{sg} being the number of signal events in a bin of the distribution and N_{bg} the amount of background in a bin. Then the signal efficiency is used as a criterion for which bin in the distribution can be chosen. The bin with the highest significance and sufficient signal efficiency has to be determined. Thereby the signal efficiency affects how tight or loose the selection is going to be, with higher efficiencies corresponding to a more loose selection and lower efficiencies corresponding to a more tight selection. Once the most significant bin with the required signal efficiency is found, the error is evaluated by choosing the two bins which are farthest away within 1σ of the chosen bin. An example with the required signal efficiency of 90% is shown in figure 5.4
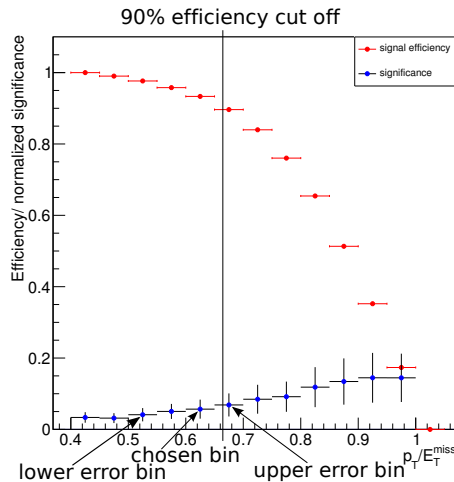
15

Figure 5.4: An example for selection process is shown: For a signal efficiency of 90% the chosen bin and the upper and lower error bin are indicated by arrows pointing at them.

Once this process is completed, a function is fitted to the resulting distribution. The effectiveness of selections is evident when comparing the M_T distribution before and after selections, using the PS_{90} selection in figure 5.5 as an example. The analogous figures for the W'_{static} and W'_{M_T} selections can be found in the appendix B. For the PS_{90} selection, the number of signal events for M_T above ≈ 600 GeV are virtually unchanged for both (P)S models, but still yield a discrepancy for the AV models. This is assumed to be an effect of the less steep shape of the AV models compared to the (P)S models in the $\Delta\phi$ distributions, in which the PS_{90} selection is the most rigorous. The fact that low M_T region for all models suffers from signal loss can be explained by the upper bound p_T/E_T^{miss} being in close proximity to the peak.

However, to be able to determine the best type of selection for this search, limits are determined using three different selections: The W'_{static} selection used in [27], the selection optimized for W' produced by AV mediators using the algorithm described and the selections optimized for dark matter produced by scalar mediators. These kinematic selections are listed in table 5.6 and visualized in figure 5.7. It can be seen that the W'_{static} selection does not change with respect to the selection variables. The W'_{M_T} selection does not change in $\Delta\phi$ and the upper bound on p_T/E_T^{miss} is fixed as well, while the lower bound is a parabola which results in no lower bound on p_T/E_T^{miss} for $M_T > 2$ TeV. For the PS_{90} selection, both, the selection of $\Delta\phi$ and the p_T/E_T^{miss} are partly M_T dependent, for $M_T < 900$ GeV p_T/E_T^{miss} can be described with a linear function in M_T and for $\Delta\phi$ the dependency is given by an error function.

The effect of the selections is further investigated in section 6.3 by determining expected cross section limits. These limits are then used to estimate possible improvements of M_T-dependent selections over static selections.
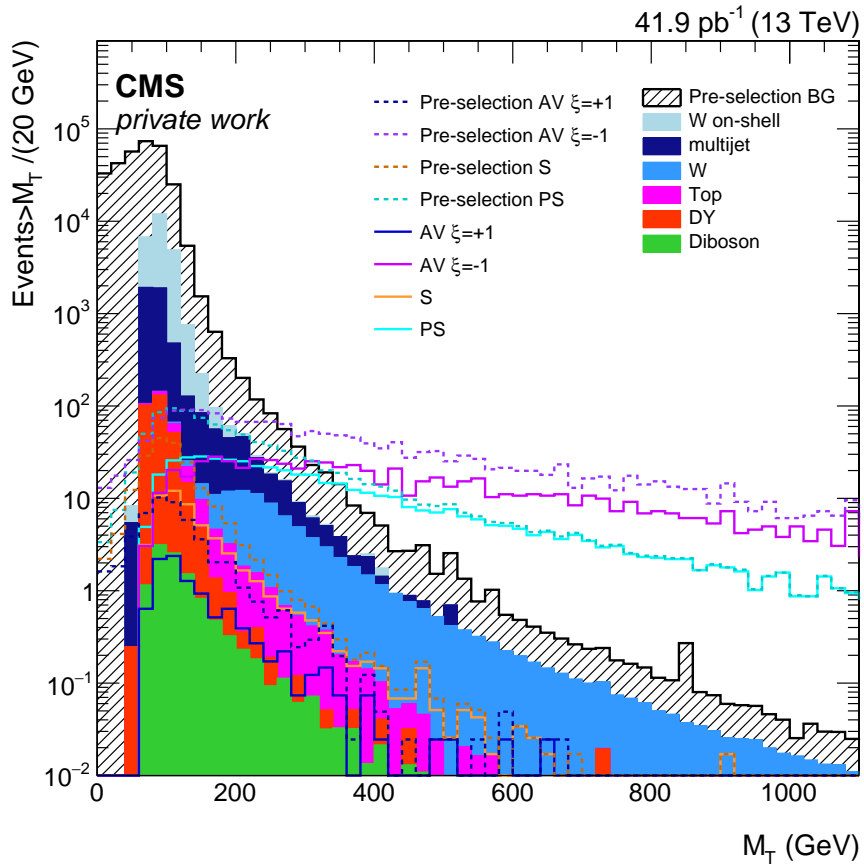
16

Figure 5.5: Comparision of M_T distributions: The filled backgrounds are after the PS_{90} selection whereas the hatched background is pre-selection. The filled bacground feature a significantly slimmed peak region. The signals are produced with M_{med}=50 GeV.

Table 5.6: The different selections are displayed; M_T is given in units of GeV.

$$W'_{static} = \begin{cases} p_T/E_T^{miss} > 0.4 \\ p_T/E_T^{miss} < 1.5 \\ \Delta\phi > 2.5 \\ \text{selection used in [27] and follow-up searches, for example [72]} \end{cases}$$

$$W'_{M_T} = \begin{cases} p_T/E_T^{miss} > 0.58 + 7.9 \cdot M_T \cdot 10^{-4} - 5.28 \cdot M_T^2 \cdot 10^{-7} \\ p_T/E_T^{miss} < 1.1 \\ \Delta\phi > 2.8 \cdot Erf(\frac{M_T+7.6}{140}) \\ \text{M_T dependent selection optimized for W'_{static} signals with a} \\ \text{required efficiency of 50\%} \end{cases}$$

$$PS_{90} = \begin{cases} p_T/E_T^{miss} > \begin{cases} 0.44 + 1.9 \cdot M_T \cdot 10^{-4}, & \text{if } M_T < 900 \\ 0.68, & \text{if } M_T > 900 \end{cases} \\ p_T/E_T^{miss} < \begin{cases} 1.43 - 4.2 \cdot M_T \cdot 10^{-4} + 1.05 \cdot M_T^2 \cdot 10^{-8}, & \text{if } M_T < 900 \\ 1.12, & \text{if } M_T > 900 \end{cases} \\ \Delta\phi > 2.963 \\ \text{M_T dependent selection optimized for pseudoscalar signals} \\ \text{with a required efficiency of 90\%} \end{cases}$$
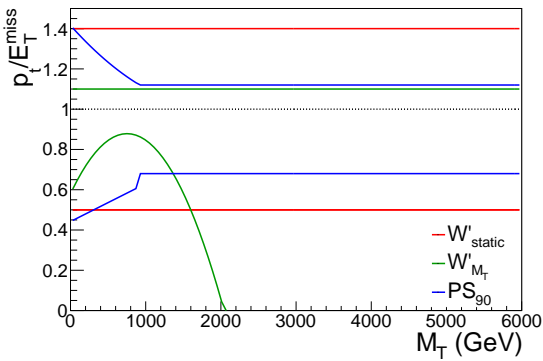
(a) resulting p_T/E_T^{miss} selections
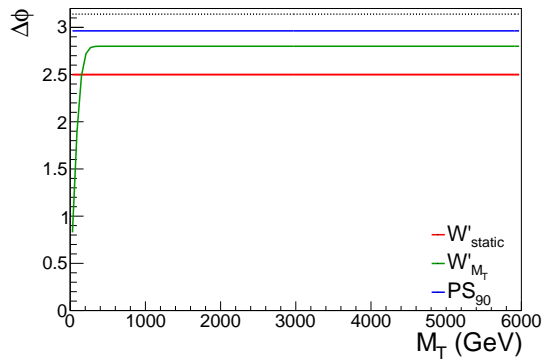
(b) resulting $\Delta\phi$ selections

Figure 5.7: Functions for the kinematic selection are shown, p_T/E_T^{miss} on the left and $\Delta\phi$ on the right.

Chapter 6

Interpretation of Results in Terms of Limits

Utilizing the three different possibilities for kinematic selection, see table 5.6, the effects of these selections on the expected limits for a (P)S or AV signal are studied. Because of the optimization of the kinematic selection being done for p_T triggers, these triggers are used to finalize the optimization. The sensitivity study uses high p_T triggers, as these are better understood than the low p_T ones. In earlier analyses, for example [27], it has been shown that V signals generally have comparable sensitivity to AV signals. However, V signals are not competitive to direct detection as vector coupling is sensitive to the number of nucleons, while the AV model is sensitive to the spin. Lastly, the sensitivity of the studied models are compared to each other and expected limits for higher integrated luminosities are computed.

6.1   Computation of Limits

In order to derive a limit from the M_T distribution, a multi-bin approach is used, similar to previous analyses, for example [71]. This is based on the shape of the M_T distribution, when kinematic selection is applied. The M_T distribution is divided into bins and for each bin the likelihood function is separately evaluated. The combination of all bins then enables the limit to be derived for each signal used. Utilizing the Higgs combine tool [73, 74] a Bayesian approach, as explained in chapter 38 of [6], with a uniform prior for both the expected and observed limits is used. The limits are obtained at 95% confidence level, with the parameter of interest being the signal cross section times branching ratio of the decay of the mediator into a dark matter pair. The branching ratio is set to 1. The derived cross section limits indicate the cross section, that a given signal is required to have, in order to exclude it. An exclusion of a signal requires the observed cross section limits to be lower than the production cross section.

As the parameter of interest is the cross section times branching ratio of this final state, the plots will show the cross section times branching ratio as a function of either the mediator mass M_{med} or as the function of the integrated luminosity $\mathcal{L}_{int}$. When comparing different kinematic selections, each selection is depicted with a line style and color, while each model has a distinct color when compared to one another, this color code is kept in all figures. When investigating a single limit, the dashed line shows the median of the expected limit, the solid line represents the observed limit, while the green and yellow bands represent the 1 and 2 σ bands. Respecting the color code used for the models in prior plots, production cross section are shown to indicate

the sensitivity of each model.

In every following sections the limits are computed using the high p_T trigger, except for section 6.3, in which the low p_T trigger is used.

6.2 Interpretations

Earlier analyses have shown [33,42] that the investigated models have an increased cross section for the narrow width approach compared to a wide width approach. These analyses also have shown that the shape of the M_T distribution does not change for different values for the width Γ, while the number of expected signal events change. Furthermore [37] has shown that the M_T shape also is not affected by using either a Majorana or Dirac assumption for the dark matter particle, while the cross section is increased by a factor of 2 for the Majorana assumption with respect to the Dirac assumption.

Utilizing the fact that the exclusion limit depends on the shape of the M_T distribution the sensitivity can be interpreted using the narrow width approach ($\Gamma = M_{med}/8\pi$) and the wide width approach ($\Gamma = M_{med}/3$) for all four models and additionally the Majorana as well as the Dirac dark matter particle assumption for the AV models.

6.3 Completion of Selection Optimization

To conclude the optimization of the kinematic selection from section 5.3, the effects of the optimized W'_{M_T} and PS_{90} selections are compared to the previously existing W'_{static} selection. This is done using low p_T triggers instead of high p_T triggers as done in sections 6.5.1 through 6.9. Owing to the fact, that the effects of the selection optimization can be seen best for high luminosities, the limits are computed for an integrated luminosity of 10 fb^{-1}, using the Bayesian approach. This integrated luminosity is expected to be recorded at the end of 2016.

Figures 6.1 and C.1 show the cross section limit for the four different models studied. It should be noted that the sigma bands are not shown. The sigma bands indicate the influence of the systematic uncertainties on the subjective degree of believe [75] in the Bayesian approach. As this section is supposed to compare the most probable and thus most trustworthy expected limits, the sigma bands are omitted.

Starting with the AV model and ξ=+1 in particular, it can be seen in figure 6.1 on the left side that the PS_{90} selection results in a higher cross section limit for low M_{med}, but a lower cross section limit for high M_{med}, compared to the W'_{static} selection. The W'_{M_T} selection in contrast provide continuously lower cross section limits than any other selection. Compared to the W'_{static} selection, the W'_{M_T} selection are an improvement of (11.3 to 14.2)% for M_{med}>500 GeV, for PS_{90} and M_{med} >500 GeV, this varies from (8.3 to 13.4)%. For low M_{med} values, however, the W'_{static} selection are 30.8% lower than W'_{M_T} and 41.4% lower than the PS_{90} selection. These values can be found in table C.1.

For ξ=-1, see figure 6.1 on the right side, the W'_{static} selection only yields a lower limit than the PS_{90} selection for high M_{med}, but yields higher limits than the PS_{90} selection otherwise. The W'_{M_T} selection yield the lowest limits for all M_{med} and are an improvement of (1.7 to 9.3)% compared to the W'_{static} selection. The difference between the W'_{static} and PS_{90} selections ranges from (-7.7 to 4.4)%, with the negative value indicating the PS_{90} selection yielding a lower limit

and the positive value indicating the W'_{static} selection to yield a lower limit. These values can be found in table C.2.
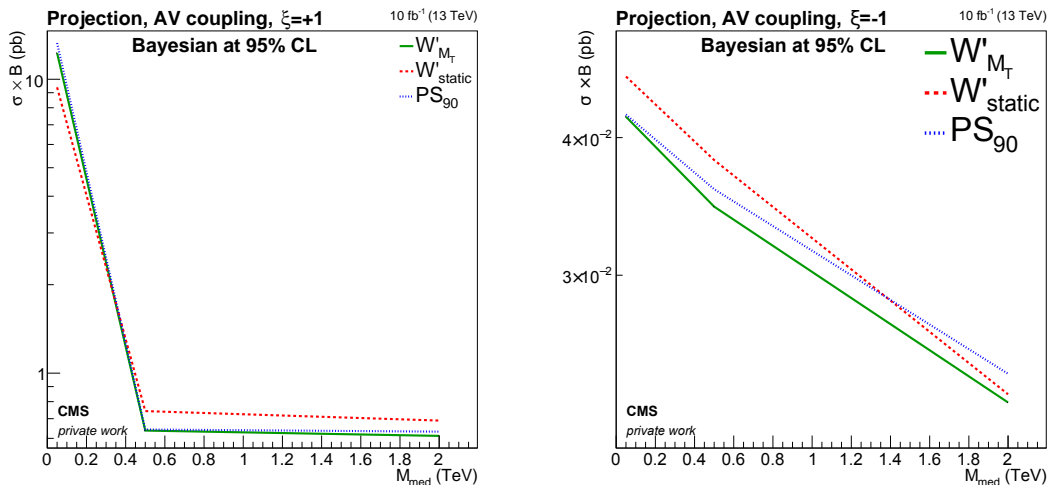
(a) AV ξ=+1   (b) AV ξ=-1

Figure 6.1: Comparision of expected limits for the three different selections and AV ξ=+1 (left) or ξ=-1 (right) signals, with the W'_{M_T} selection yielding the lowest limit both cases.

In the S model, see figure 6.2 on the left side, the W'_{static} selection yields the highest cross section limits with the exception of low M_{med}, for which the W'_{M_T} selection yields slightly higher limits. Similar to the W'_{M_T} selection for the AV models, the PS_{90} selection provide continuously lower cross section limits than any other selection tested for the S model. The PS_{90} selection is an improvement of (22.3 to 24.3)% in relation to the W'_{static} selection for $M_{med}>500$ GeV; for the W'_{M_T} selection, this ranges from (22.9 to 25.3)%. In case of $M_{med}<500$ GeV, the PS_{90} selection yield 7.1% and the W'_{M_T} selection 11.4% higher cross section limits. These values can be found in table C.3.

Lastly, for an PS signal, see figure 6.2 on the right side, the W'_{static} selection yields in the tested M_{med} region higher cross section limits than both the W'_{M_T} and PS_{90} selections. The latter mentioned pair of selections yield nearly the same limits, with the W'_{M_T} selection leading to slightly lower limits until high M_{med}, for which the PS_{90} and W'_{M_T} selections yields approximately the same limits. The W'_{M_T} selection are overall an improvement of (20.9 to 38.1)% relative to the W'_{static} selection and the PS_{90} selection are an improvement of (21.2 to 38.1)%. These values can be found in table C.4.

6.3.1 Conclusion

The W'_{M_T} selection is an improvement for all models studied, neglecting the low M_T region in the AV ξ=+1 case. This improvement is in the order of 5 to 10% for both AV models and at least of the order of 20% for the (P)S models. The PS_{90} selection proves to be comparable to the W'_{M_T} selection for the (P)S and the AV ξ=+1 models, but is worse for the AV ξ=-1 model. This result shows that an optimization regarding the M_T-dependency of the selection is of good value. However, once an M_T-dependent selection has been produced for a similar signature, a dedicated optimization yields only little improvement.
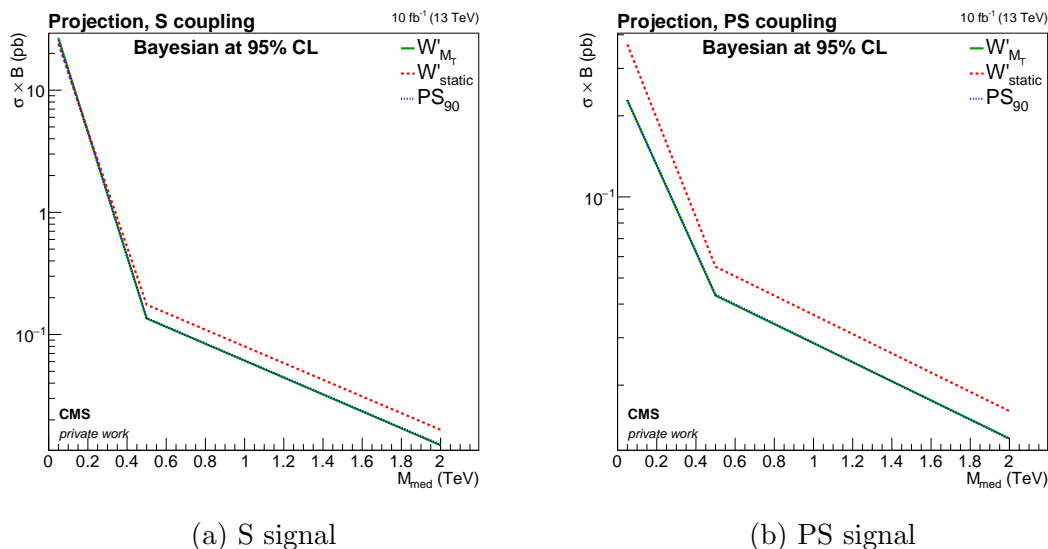
21

Figure 6.2: Comparision of expected limits for the three different selection and S (left) or PS (right) signals, the W'_{M_T} selection yielding the lowest limit in the PS case and the PS_{90} selection yielding the lowest limits in the S case.

6.4 Prediction of Limits for high p_T Triggers

In figure 6.3 the signals are shown for each mediator mass. For M_{med}=50 GeV every signal is distinguishable due to different shapes. Despite differences in shape, the PS and the AV ξ=-1 signal are comparable, as both the peak height and the slope are comparable, with PS having a less steep slope. Analogously the S and AV ξ=+1 signals are comparable. While the same observation can be made for M_{med}=500 GeV, the S and AV ξ=+1 signals have a higher slope, which is getting comparable with those of the AV ξ=-1 and PS signals. For M_{med}=2000 GeV the AV ξ=+1 is approximately the same as for M_{med}=500 GeV, however, the PS, S and AV ξ=-1 signals have roughly the same shape and slope. As a result of the much lower cross section for the PS and S cases, discrepancies in event numbers between the three mentioned signals can be observed, especially for high M_{med}.

As a consequence of the AV ξ=-1 signal not changing its shape nor the slope changing drastically, it is to be expected, that correspondingly the cross section limit does not change much. The S signal, in contrast, changes drastically in shape and slope, so that it can be assumed, that the cross section limit will decrease drastically with increasing M_{med}. A similar assumption can be made for the PS case; the cross section limit will decrease as a function of M_{med}. In contrast it is anticipated that the S signal will decrease more quickly. This is due to the fact that the M_T shape drastically changes as a function of M_{med}. The cross section limit for the AV ξ=+1 case is for the same reason expected to decrease as a function of M_{med}, but becoming stagnant for M_{med}>500 GeV as the shape does not change much.

Based on the flat shape in M_T in the PS, AV ξ=-1 and S cases, assuming a mediator with high M_{med}in the S model, the high M_T region is most influential, while for the AV ξ=+1 and low M_{med} S models the low M_T region is most influential.

As a result of the scalar mediator coupling to an exited W boson instead of the coupling to quarks in the initial state, the production cross section is extremely small for mediator masses

M_{med}>500 GeV. This leads to an extremely small number of events for the (P)S models, thus a very large integrated luminosity is needed in order to have a measureable event expectation from this process. Due to this fact the (P)S models will most likely only be sensitive to low mediator masses M_{med}.
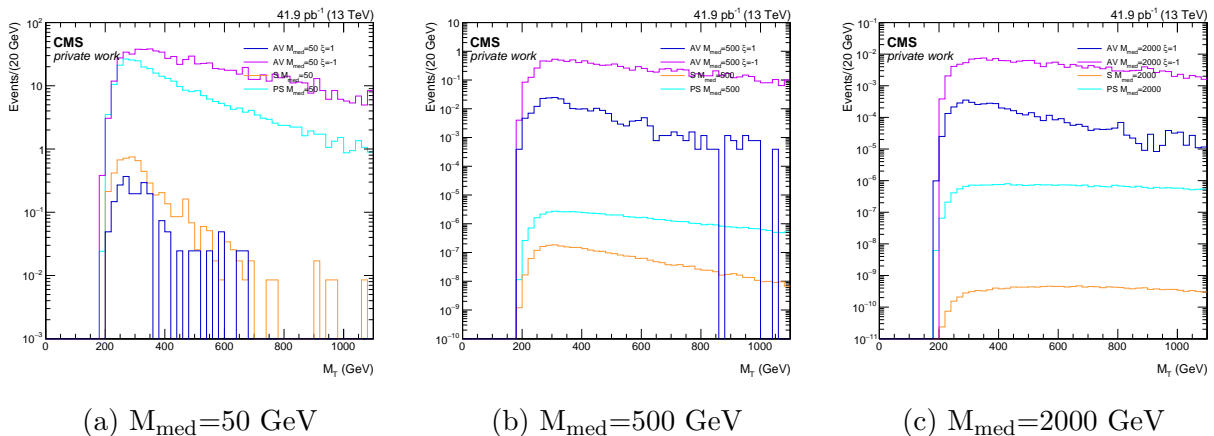

(a) M_{med}=50 GeV

(b) M_{med}=500 GeV

(c) M_{med}=2000 GeV

Figure 6.3: M_T distributions for the considered models after kinematic selection and triggers are applied. From left to right, the mediator mass increases from 50 to 2000 GeV.

6.4.1 Discussion of M_T distributions

The effects on the number of events above 500, 1000 and 1400 GeV in M_T for the PS signal, M_{med}=50 GeV and the three possible selections from table 5.6, are given in table 6.1 and visualized in figure 6.4, taking M_T>200 and 300 GeV into account as well. Additionally, tables showing the number of events and statistical uncertainty for all M_{med} of the studied signals, the background and selections used with high p_T triggers applied are given in the appendix D. The right side of figure 6.4 shows that the W'_{static} selection are the least aggressive, thus the most signal events remain. However, the signal to background ratio in turn is the smallest, as seen in the left side of figure 6.4. In contrast the W'_{M_T} and PS_{90} selections are the most aggressive, which leads to higher signal to background ratio for the full M_T region. When considering only M_T >1000 GeV, the PS_{90} selection yield the highest signal to background ratio. These findings imply that with increasing integrated luminosity the PS_{90} selection will yield increasingly lower limits than the other selections, as for increasing integrated luminosities more high M_T events are expected.

In the top row of figure 6.5 the M_T distribution for each kinematic selection is shown. The W'_{static} selection result in both the most signal and background, while the PS_{90} selection result in the least background. The PS_{90} selection produces the same shape of the background for low M_T as the W'_{static} selection, namely a broad peak, but has a more steep slope for high M_T. The W'_{M_T} selection have approximately the same slope for high M_T, yet for low M_T the shape changes with respect to both PS_{90} and W'_{static} selections. The peak has approximately the same peak height compared to the W'_{static} selection, however, the peak has slimmed down.

23

Table 6.1: Effects of the different selections on the number of signal (N_{signal}) and background events ($N_{SM\,bg}$) for $M_T>$ 500, 1000 and 1400 GeV for a PS signal with M_{med}=50 GeV and the signal to SM background ratio ($\frac{N_{signal}}{N_{SM\,bg}}$) for the respective selection are displayed. The error on the number of events is the statistical error.

| PS M_{med}=50 GeV	kinematic selection	M_T threshold		
		$M_T>$500 GeV	$M_T>$1000 GeV	$M_T>$1400 GeV
N_{signal}	W'_{static}	107.8 ± 1.6	21.87 ± 0.73	7.90 ± 0.44
$N_{SM\,bg}$		3.49 ± 0.20	0.1908 ± 0.0028	$385.5 \pm 2.1 \cdot 10^{-4}$
$\frac{N_{signal}}{N_{SM\,bg}}$		22.0	88.8	163.6
N_{signal}	PS_{90}	103.1 ± 1.6	21.78 ± 0.73	7.90 ± 0.44
$N_{SM\,bg}$		4.89 ± 0.25	0.2462 ± 0.0055	0.0483 ± 0.0027
$\frac{N_{signal}}{N_{SM\,bg}}$		29.5	114.2	204.9
N_{signal}	W'_{M_T}	94.6 ± 1.5	21.63 ± 0.72	7.88 ± 0.44
$N_{SM\,bg}$		2.87 ± 0.16	0.1954 ± 0.0028	$404.8 \pm 2.2 \cdot 10^{-4}$
$\frac{N_{signal}}{N_{SM\,bg}}$		32.9	110.7	194.7
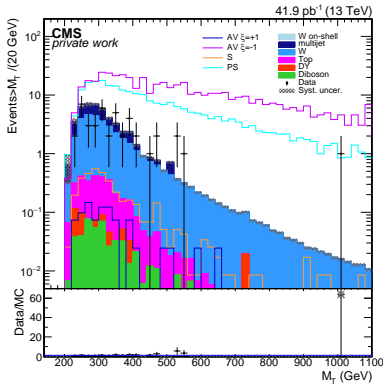
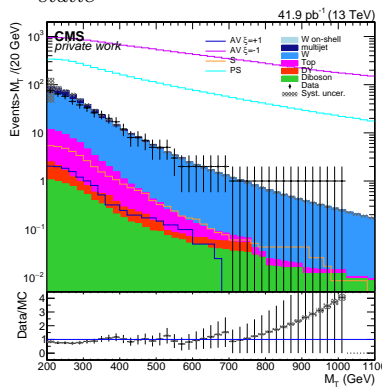(a) M_T distribution after PS_{90} kinematic selection
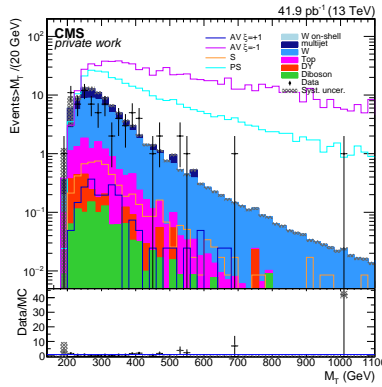
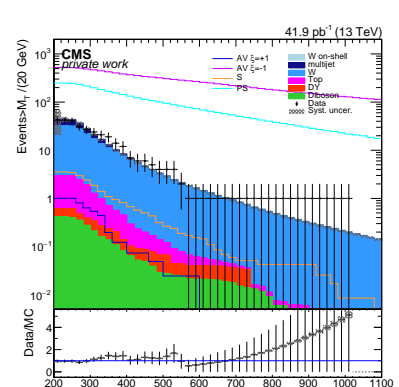(b) M_T distribution after W'_{static} kinematic selection
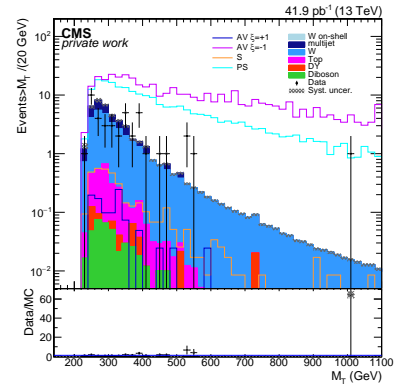
(c) M_T distribution after W'_{M_T} kinematic selection
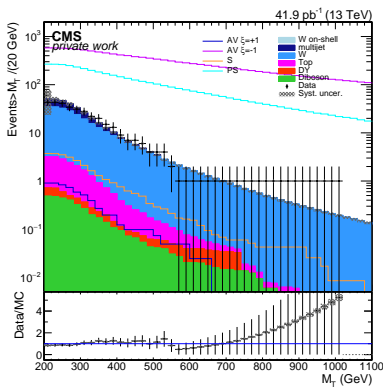
(d) cumulative M_T distribution after PS_{90} kinematic selection

(e) cumulative M_T distribution after W'_{static} kinematic selection

(f) cumulative M_T distribution after W'_{M_T} kinematic selection

Figure 6.5: M_T distributions with kinematic selection and triggers applied are shown, in the bottom row the M_T distribution is displayed cumulatively. The signals are produced with M_{med}=50 GeV.
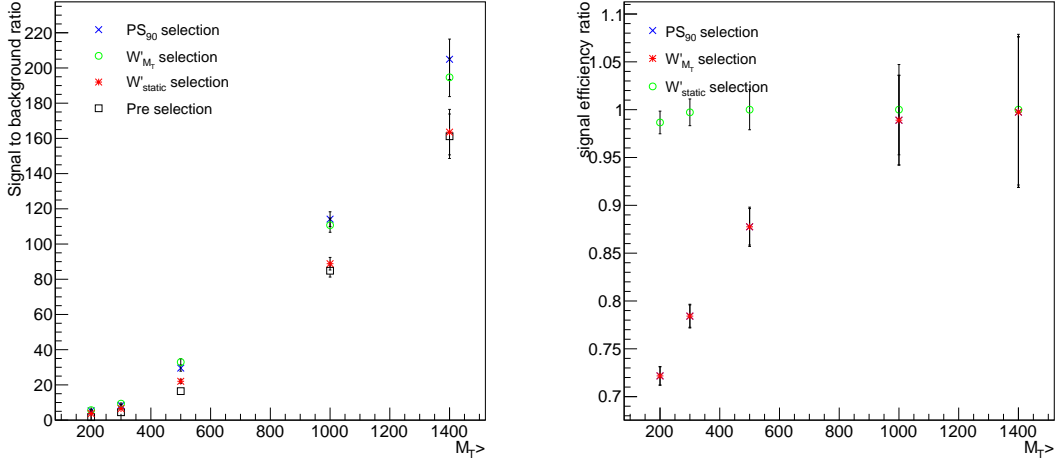
Figure 6.4: Signal to background ratio on the left and signal efficiency on the right for the PS model and M_{med}=50GeV. For high M_T PS_{90} selection provides best signal to background ratio, but suffers from turn on in signal efficiency. In contrast W'_{static} selection provides the worst improvement over the preselection but barely loses any signal events. Uncertainty on signal to background ratio is the gaussian propagated statistical uncertainty of the number of signal and background events respectively.

All of the M_T distributions share one feature, as they show disagreement between data and Monte Carlo prediction. Depending on which kinematic selection is applied and depending on the region of M_T either under or over fluctuation can be observed. This is partly due to corrections on E_T^{miss}, especially the jet energy corrections are not final. As this analysis intends to focus on the sensitivity of the (P)S model and prepare a possible follow-up analysis on the complete set of data taken in 2015, this disagreement will be investigated in this future analysis. The last point also explains why this analysis is only using three mediator mass points. The understanding of mentioned jet energy corrections is expected to improve for the data taken with 25 ns bunch spacing along side the understanding of the detector.

In the bottom row of figure 6.5 the M_T distribution for each kinematic selection is shown in a cumulative plot. In a cumulative plot for a given variable, for example M_T, a bin, that is located at a specific M_T value contains the total number of events that have the same or a higher M_T value. This type of visualization can be used to show discrepancies between the data taken and the SM expectation.

The cumulative M_T distributions show that the agreement is dependent on the kinematic selection. While for the W'_{static} selection the data has a fair agreement for cumulative M_T bigger than 300 GeV, shows disagreement for M_T below that value. While the W'_{M_T} selection has a fair agreement for all M_T, the PS_{90} selection shows a decent agreement of data and background, especially for early data. All three selection have regions in which an over or under fluctuation can be found.

25

6.5 Comparison of Different Kinematic Selections

As a consequence of the overall vastly different shape of the MT distribution in compared to 5.5, it can to be assumed, that the conclusion stated in subsection 6.3.1 is not true for high p_T-triggers. Following this assumption the effects of the different kinematic selections are compared for high p_T-triggers. The most effective kinematic selection is then used to compute the observed as well as the projected expected limits in the following sections.

6.5.1 Pseudoscalar coupling

In figure 6.6 the expected limits at an integrated luminosity of $\mathcal{L}_{int}=$ 41.9 pb^{-1} are shown. While all three selections are decreasing in cross section with the mediator mass, the W$'_{static}$ selection varies from the other two with respect to the behavior between 50 and 500 GeV. This difference is a steeper slope in this region. The cross section limit for the W$'_{static}$ selection continues to decline at roughly the same rate as both PS$_{90}$ and W$'_{M_T}$ for M$_{med}$ > 500 GeV.

For all M$_{med}$ the W$'_{static}$ selection yields the lowest expected limits, while both PS$_{90}$ and W$'_{static}$ yield nearly the same limit. Using the W$'_{static}$ selection is an improvement of (2.4 to 26.0)% compared to the PS$_{90}$ selection and (-1.0 to 24.5)% compared to the W$'_{M_T}$ selection. The factors can be found in table 6.2.
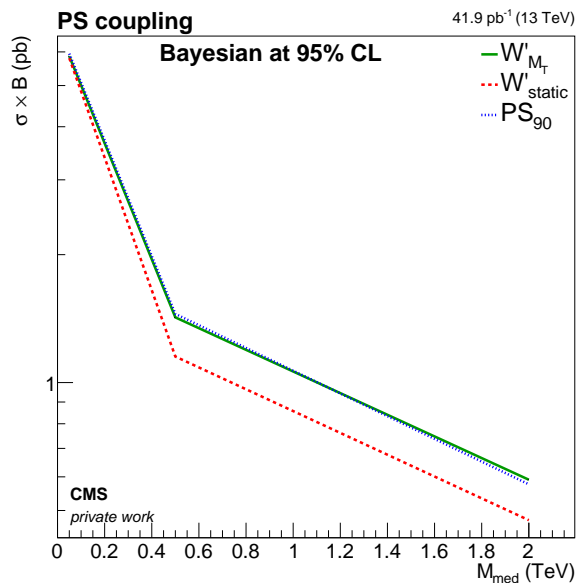

Figure 6.6: Comparision of expected limits for the three different selections and a PS signal, W$'_{static}$ yielding the lowest limit.

Table 6.2: Cross section limits for a PS signal are given for each mediator mass point M_{med} and kinematic selection and are compared to the W'_{static} selection.

name \ M_{med}	σ_{limit} [pb]		
	50 GeV	500 GeV	2000 GeV
W'_{static} in pb	5.80	1.15	0.47
PS_{90} in pb	5.94	1.45	0.58
comp. to W'_{static}	1.02	1.26	1.21
W'_{M_T} in pb	5.86	1.42	0.59
comp. to W'_{static}	0.99	1.24	1.25

6.5.2 Axial-vector coupling

In figure 6.7 on the left the limits of an AV signal in the case of ξ=-1 exhibit the same behavior for all the selections, namely a steady drop in cross section, which amounts to approximately 1 pb. In accordance with the limits for the PS model, the W'_{static} selection yields the lowest limits for the ξ=-1 model. The PS_{90} selection yields the next higher cross section limits, while the W'_{M_T} selection yields the highest limits.

In case of ξ=+1, see figure 6.7 on the right, The W'_{static} selection again yields the lowest limits, with the PS_{90} selection yielding the highest limits for low M_{med}, while for medium and high M_{med} the W'_{M_T} selection yield the highest limits. The PS_{90} selection varies in shape from both other possibilities, especially for low M_{med}, at which The PS_{90} selection have the steepest slope.

For M_{med} >500 GeV the limit becomes stagnant, which is due to the M_T shape not changing between 500 and 2000 GeV in M_{med}, as shown in section 6.4. Depending on the mediator mass M_{med}, using the W'_{static} selection is an improvement of (69.9 to 72.2)% compared to the PS_{90} selection and (87.3 to 105.4)% compared to the W'_{M_T} selection for ξ=-1. For the ξ=+1 case the W'_{static} selection is an improvement of (34.0 to 325.1)% compared to the PS_{90} selection and (55.6 to 67.6) % compared to the W'_{M_T} selection. In table 6.3 the comparison of kinematic selections is shown in reference to the W'_{static} selection for ξ=-1 and ξ=+1 respectively in terms of factors.
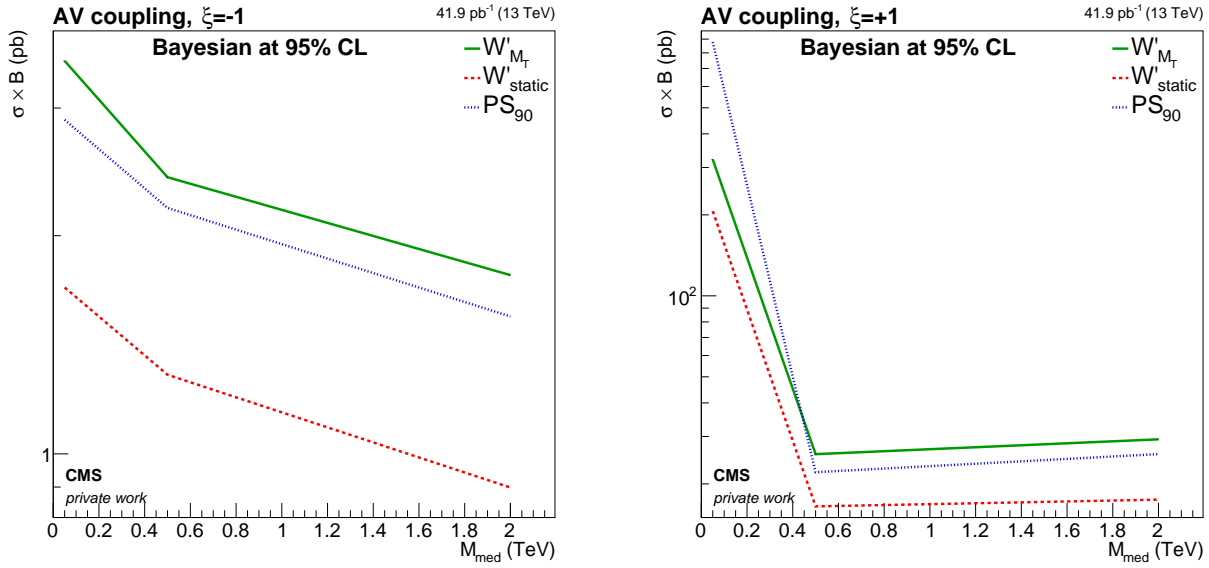
Figure 6.7: Comparision of expected limits for the three different selections and an AV signal, $\xi=+1$ on the right and $\xi=-1$ on the left. The W$'_{static}$ selection yield for both values of ξ the lowest limit.

Table 6.3: Cross section limits in pb for a AV $\xi=\pm1$ signal are given for each mediator mass point M$_{med}$ and kinematic selection and compared to the W$'_{static}$ selection.

name \ M$_{med}$	50 GeV	500 GeV	2000 GeV
AV $\xi=-1$			
W$'_{static}$ in pb	1.70	1.29	0.899
PS$_{90}$ in pb	2.89	2.18	1.54
comp. to W$'_{static}$	1.70	1.70	1.72
W$'_{M_T}$ in pb	3.48	2.41	1.76
comp. to W$'_{static}$	1.05	1.87	1.96
AV $\xi=+1$			
W$'_{static}$ in pb	206.5	16.49	17.47
PS$_{90}$ in pb	878.0	22.1	25.8
comp. to W$'_{static}$	3.25	1.34	1.47
W$'_{M_T}$ in pb	321.3	25.8	29.3
comp. to W$'_{static}$	1.56	1.56	1.68

6.5.3 Scalar coupling

For an S signal, the shape of the limits, see figure 6.8, are similar for all three sets of selection. While the cross section limit approximately diminishes two orders of magnitude between 50 and 500 GeV in mediator mass, the limit decreases roughly a third of an order of magnitude between 500 and 2000 GeV mediator mass. Similar to the PS and AV limits, the W'_{static} selection yield the lowest limits, while similar to the PS model and in contrast to the $\xi=\pm1$ cases, the PS_{90} and W'_{M_T} selections yield approximately the same and highest limits.

Using the W'_{static} selection is an improvement of (15.9 to 26.0)% compared to PS_{90} selection and (19.6 to 29.9)% compared to the W'_{M_T} selection. In table 6.4 the comparison of the selections is shown in reference to the W'_{static} selection.
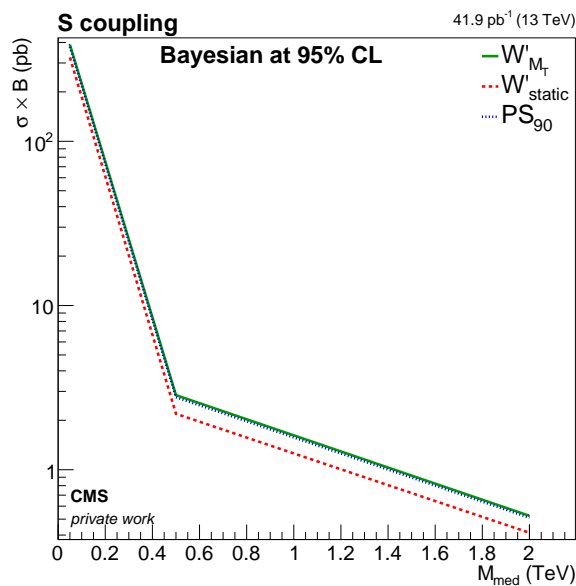

Figure 6.8: Comparision of expected limits for the three different selecions and a S signal with the W'_{static} selection yielding the lowest limit.

Table 6.4: Cross section limits in pb for a S signal are given for each mediator mass M_{med} and kinematic selection and compared to the W'_{static} selection.

name \ M_{med}	σ_{limit} [pb]		
	50 GeV	500 GeV	2000 GeV
W'_{static} in pb	324.20	2.19	0.41
PS_{90} in pb	375.86	2.76	0.510
comp. to W'_{static}	1.16	1.26	1.23
W'_{M_T} in pb	387.7	2.85	0.524
comp. to W'_{static}	1.20	1.30	1.27

6.6 Comparison of the Different Models

As subsections 6.5.1 through 6.5.3 have shown, the W'_{static} selection continuously provides the best limits, thus the sensitivity of the different models will be studied using the selections specified in table 5.6. This is in contrast to the result from section 6.3, which showed that a M_T-dependent selection yields lower cross section limits. This discrepancy can be explained by the fact that different triggers were used for the comparisons, showing the sensitivity to the used trigger in section 6.3.

Figure 6.9 illustrates that the AV ξ=-1 model for low mediator masses M_{med} is approximately a factor 200 lower than S and AV ξ=+1 and a factor 3 with respect to PS signals, while at medium mediator masses both S and PS limits are in the same order of magnitude and even yielding a factor 2 lower cross sections limits for high M_{med}. In contrast the AV ξ=+1 model yields a limit that is a factor 10 bigger in cross section due to differences in shape.

This behavior is expected, as section 6.4 has shown, that the shape of the signal for the different models changes with increasing mediator masses, resulting in the M_T distribution shifting to higher values, see 6.3.

Considering the production cross sections seen in figure 2.6, it is evident, that for 41.9 pb^{-1} of integrated luminosity, CMS is potentially sensitive to a wide range of mediator masses M_{med} for AV ξ=-1, while being only sensitive to low M_{med} in the (P)S cases and being not yet sensitive to AV ξ=+1 signals.
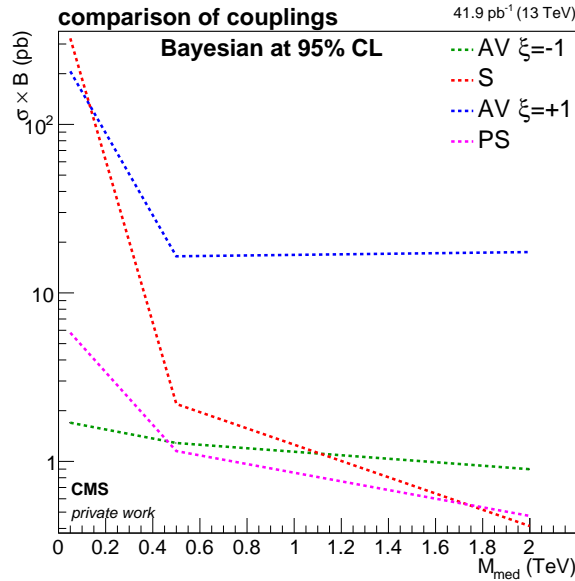

Figure 6.9: Comparision of models using the W'_{static} selection.

6.7 Observed Limits

Until now, the discussion of expected exclusion limits is based on the simulated backgrounds and signal files, however, the data taken in run B can be used to determine the observed limits. In figures 6.10 (a) through (d), these observed limits are shown using the W'_{static} selection. The markers in this figure indicate the simulated mediator mass points.

It can be seen, that the observed limits are at consistently within $2\ \sigma$ of the expected limits. While for AV ξ=-1 there is a constant over fluctuation, for ξ=+1 there is a constant under-fluctuation. This can be explained by considering the influential M_T regions. For the ξ=-1 case the high M_T region is most influential, for which less events are predicted than observed, see figure 6.5e. In the case of ξ=+1, however, the most influential region is the low M_T region, in which less events are observed than expected.

A comparable behavior is found for the PS signal, with PS showing an over fluctuation, which can be explained analogously to the over fluctuation of the AV ξ=-1 case. In contrast S is showing under-fluctuation for low M_{med}, developing into an over fluctuation for high M_{med}. This is compatible with the change of signal shape in M_T with M_{med} in the S model, so that for low mediator masses M_{med} low transeverse masses M_T are important, yet for increasing M_{med} increasingly high M_T is important. As the number of events prediction changes from an under-fluctuation to an over fluctuation, this is expected behavior.

In the AV ξ=-1 and PS models the production cross section and the observed limit intersect as can be seen in figure 6.10 (a) and (c). As a result the CMS detector is sensitive to these models with an integrated luminosity $\mathcal{L}_{int}$ of 41.9 pb^{-1}. In the PS model a mediator mass of $M_{med} < 155$ (85) GeV can be excluded for a width $\frac{\Gamma}{M_{med}}$ of $\frac{1}{8\pi}$ ($\frac{1}{3}$) of the mediator.

For the AV ξ=-1 model $M_{med} < 500$ (780) GeV can be excluded for the Dirac (Majorana) assumption and a mediator width $\frac{\Gamma}{M_{med}}$ of $\frac{1}{3}$, for $\frac{\Gamma}{M_{med}}$ of $\frac{1}{8\pi}$ 1880 GeV for the Dirac assumption can be excluded. When assuming the dark matter to be Majorana particles, it can be seen, that the intersection point is beyond 2 TeV in M_{med}. In order to conservatively estimate the exclusion limit, the cross section limit for $M_{med} = 2$ TeV is assumed to not change for increasing M_{med} and the intersection point is determined. Using this approach a mediator mass larger than 2160 GeV can be excluded for a mediator width $\frac{\Gamma}{M_{med}}$ of $\frac{1}{8\pi}$ in the Majorana approach.

In contrast, there is no intersection point of the production cross section and the observed limit for the AV ξ=+1 and S models, see 6.10 (b) and (d). Thus there is no sensitivity to these models with an integrated luminosity $\mathcal{L}_{int}$ of 41.9 pb^{-1}.

These findings are in good agreement with the assumption made in section 2.3. It has been assumed that the higher differential cross sections of the PS model compared to AV ξ=+1 and S models, respectively, indicates a better sensitivity. This has been confirmed by the fact that CMS is sensitive to the PS model while not being sensitive to the AV ξ=+1 and S models.
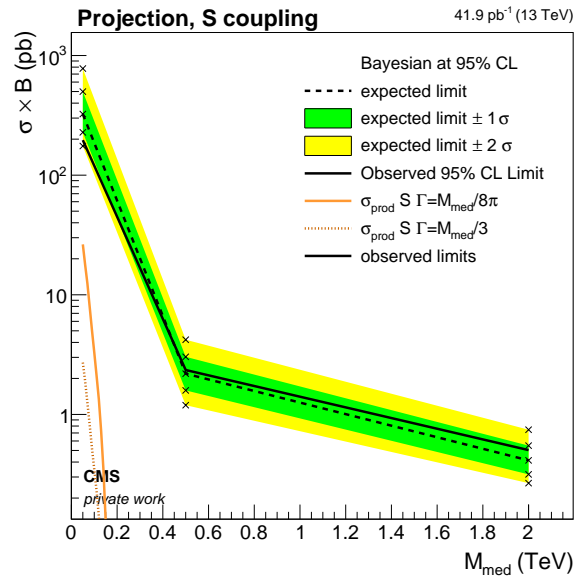
(a) AV ξ=-1
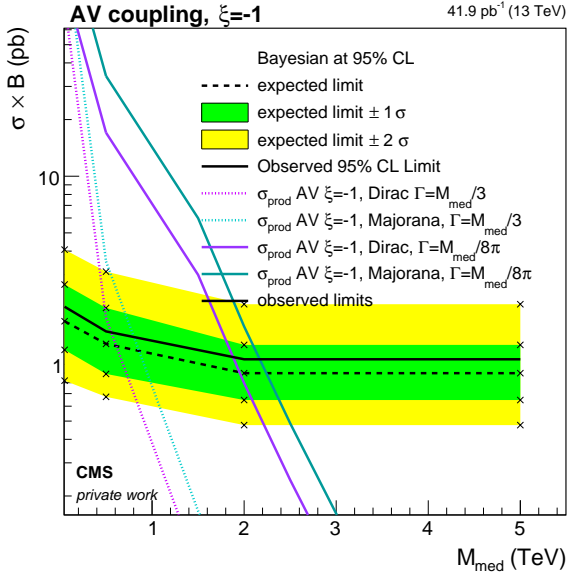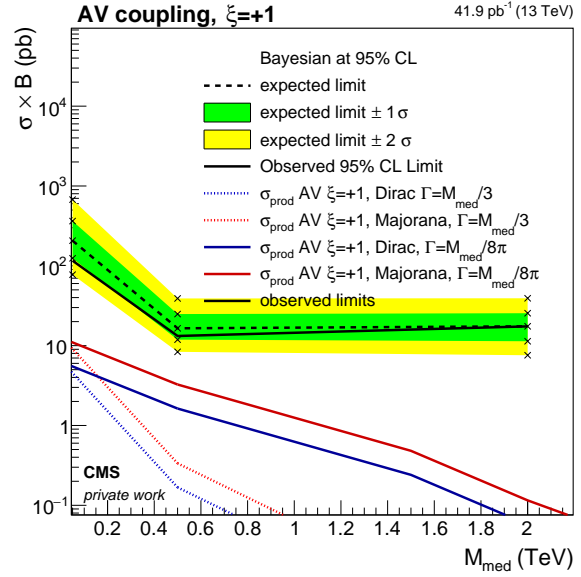
(b) AV ξ=+1
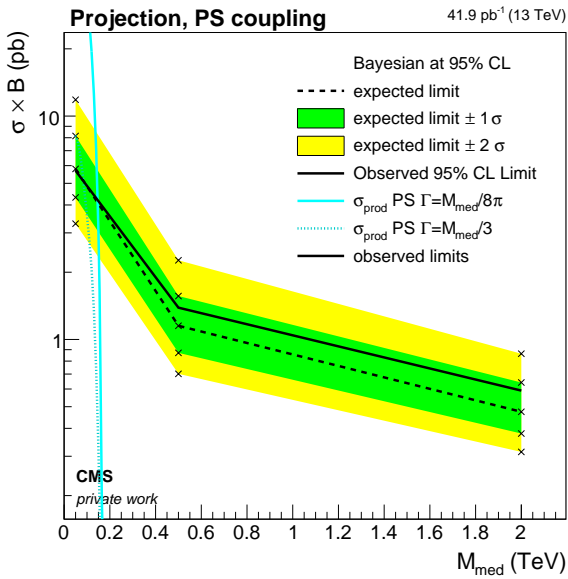
(c) PS

(d) S

Figure 6.10: Comparison of observed limits for all signals using the W′$_{static}$ selection. In green and yellow, the 1 and 2 σ bands are shown.

6.8 Comparison of Approaches

In figure 6.11 the expected limits are shown for both approaches, asymptotic and Bayesian. Unlike the Bayesian approach, the asymptotic approach does not integrade the likelihood ratio, but computes the likelihood ratio based on a single test statistic, called the Asimov set [76]. Due to this, the asymptotic approach is much less computationally demanding and results in less computing time used. As the asymptotic approach is an approximation for a big number of signal events, datasets with small amounts of data can be problematic and yield wrong results. This is due to the fact that little amounts of data only contain few signal events and thus the approximation is not fulfilled.

In figure 6.11 it can be seen, that the order of magnitude for all models and mediator mass points are in good agreement between the Bayesian and the asymptotic approach. Even though the shapes of the asymptotic approach does resemble those of the Bayesian one, it does differ. For both, AV ξ=-1 and PS signals, the disagreement between the different approaches increases, while for S and AV ξ=+1 signals, the disagreement decreases between M_{med}=50 GeV and 500 GeV, but increases for M_{med}>500 GeV again. The difference between the two approaches ranges from (-3.0 to 15.1)% for the PS model, while it varies for the S model from (2.8 to 12.8)%. In the AV ξ=+1 model, the range spans from (-3.3 to 13.1)%, while for the ξ=-1 case, it is (3.9 to 9.0)%. Figure 6.12 illustrates, that disagreement is covered well within the uncertainties of the approaches. Additionally, the uncertainties for the Bayesian approach are bigger than for the asymptotic approach in order to compensate for the disagreement.

In appendix E.1 the asymptotic limit plots can be found for all studied selections and models other than the PS model.
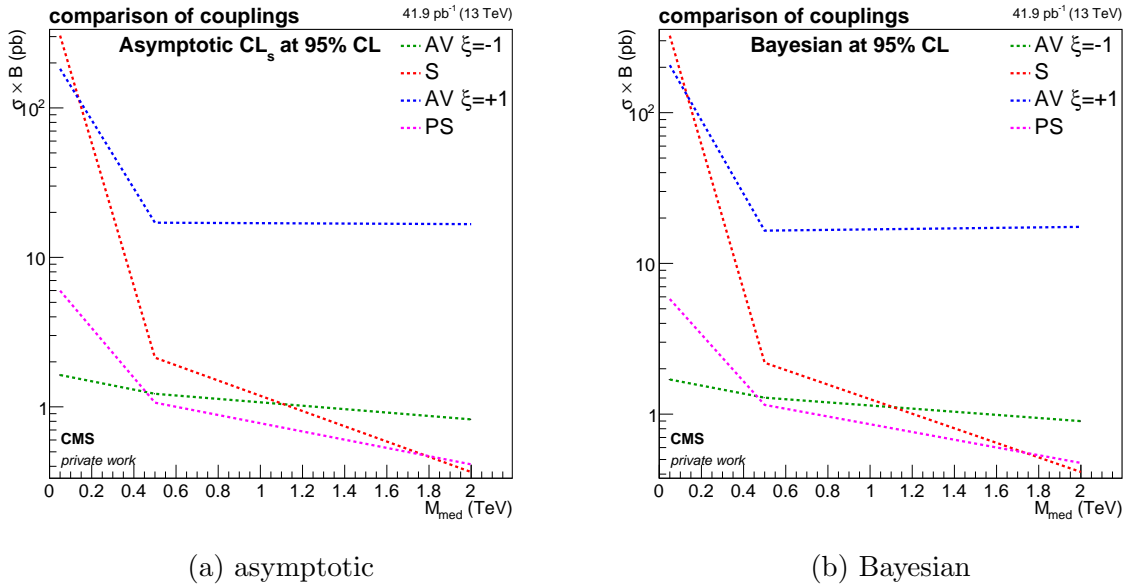

(a) asymptotic   (b) Bayesian

Figure 6.11: Comparision of methods: in the left plot asymptotic limits are shown, in the right plot Bayesian limits. For both methods the W'_{static} selection is used to compute the limits.
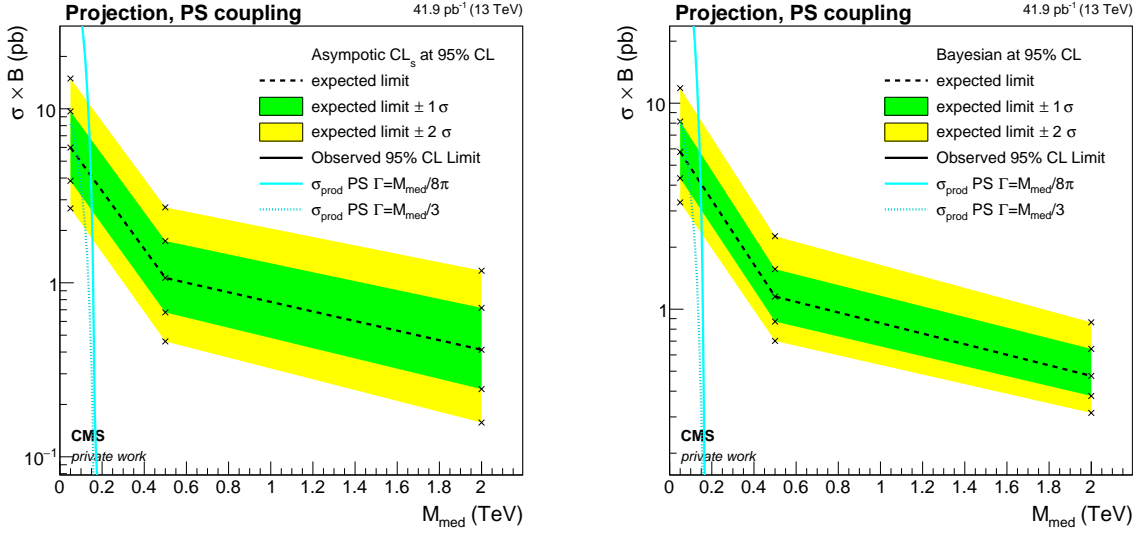
Figure 6.12: Comparision of methods for the W'_{static} selection and a PS signal: on the left are aymptotic limits and on the right are Bayesian limits for 41.9 pb^{-1}.

Table 6.5: Ratio of asymptotic cross section limit with the Baysian one.

M_{med} ratio	50 GeV	500 GeV	2000 GeV
PS_{asym}/PS_{Bayes}	0.970	1.080	1.151
S_{asym}/S_{Bayes}	1.064	1.028	1.128
AV_{asym}/AV_{Bayes} $\xi=+1$	1.131	0.967	1.047
AV_{asym}/AV_{Bayes} $\xi=-1$	1.039	1.052	1.090

6.9 High Luminosity Projection

With an integrated luminosity $\mathcal{L}_{\text{int}}$ of 2.2 fb^{-1} already being certified for all analyses and 3.8 fb^{-1} being delivered by LHC, this section will give an outlook for expected limits for integrated luminosities of 1, 3 and 10 fb^{-1}.

In figure 6.13 the expected limits can be seen for an integrated luminosity $\mathcal{L}_{\text{int}}$ of 1 fb^{-1} for all four models. The shape of the limits does not change, but the value of the cross section limit does. As figure 6.14 shows for each single mediator mass point M_{med}, the cross section limits decrease linearly with increasing integrated luminosity. In order to estimate the expected sensitivity, figure 6.15 shows the expected limits for an integrated luminosity $\mathcal{L}_{\text{int}}$ of 10 fb^{-1} and all four models.

The limits for 3 fb^{-1} can be found in E.2, the analogous plots to figure 6.14 can be found in E.3 in case of M_{med}=50 GeV for the AV models, M_{med}=500 GeV for the (P)S models and in E.4 in case of M_{med}=2000 GeV.

The intersection point of the theoretical production cross section and the expected cross section limit graph indicate the mediator mass M_{med} which is expected to be excluded for a given integrated luminosity. For 10 fb^{-1}, both, the S model is not yet sensitive for a width of $\frac{\Gamma}{M_{\text{med}}} = \frac{1}{3}$ but is expected to be able to exclude mediators with masses $M_{\text{med}} < 64$ GeV and a width of $\frac{\Gamma}{M_{\text{med}}} = \frac{1}{8\pi}$. In the AV ξ=+1 case, there is no sensitivity for $\frac{\Gamma}{M_{\text{med}}} = \frac{1}{3}$ assuming Dirac particles, but it is expected, that Majorana particles can be excluded for mediators with masses $M_{\text{med}} < 280$ GeV. For $\frac{\Gamma}{M_{\text{med}}} = \frac{1}{8\pi}$ both assumptions are expected to be sensitive and to be able to exclude $M_{\text{med}} < 1120$ (1500) GeV for Dirac (Majorana) particles. In the AV ξ=-1 model, for $\frac{\Gamma}{M_{\text{med}}} = \frac{1}{3}$ mediator masses $M_{\text{med}} < 2280$ (2660) GeV with a Dirac (Majorana) assumption are expected to be excluded. These values increase for $\frac{\Gamma}{M_{\text{med}}} = \frac{1}{8\pi}$ to $M_{\text{med}} < 4090$ (4670) GeV for Dirac (Majorana) particles. In the PS model mediator masses $M_{\text{med}} < 170$ (157) GeV are expected to be excluded for a width of the mediator of $\frac{\Gamma}{M_{\text{med}}} = \frac{1}{8\pi}$ ($\frac{\Gamma}{M_{\text{med}}} = \frac{1}{3}$).
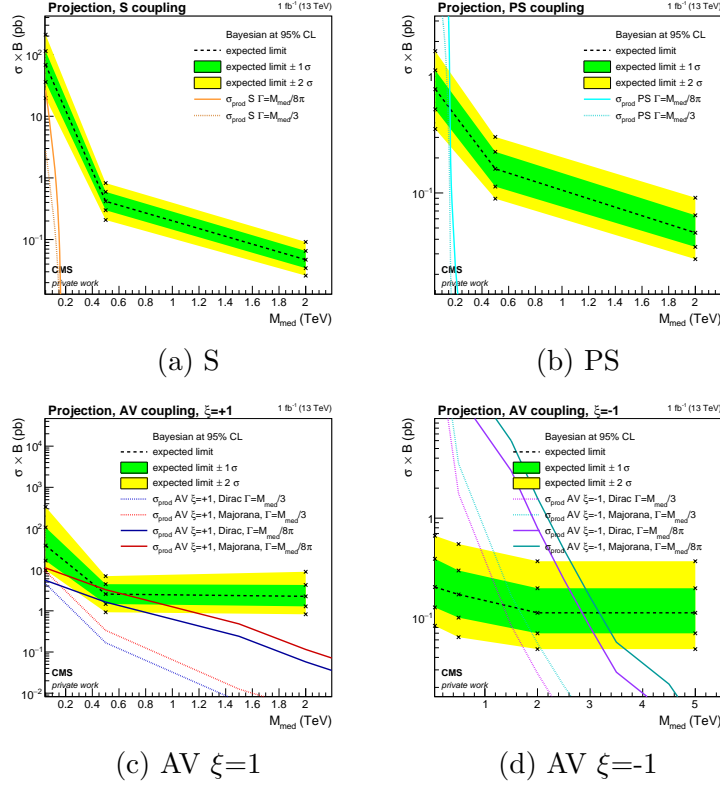
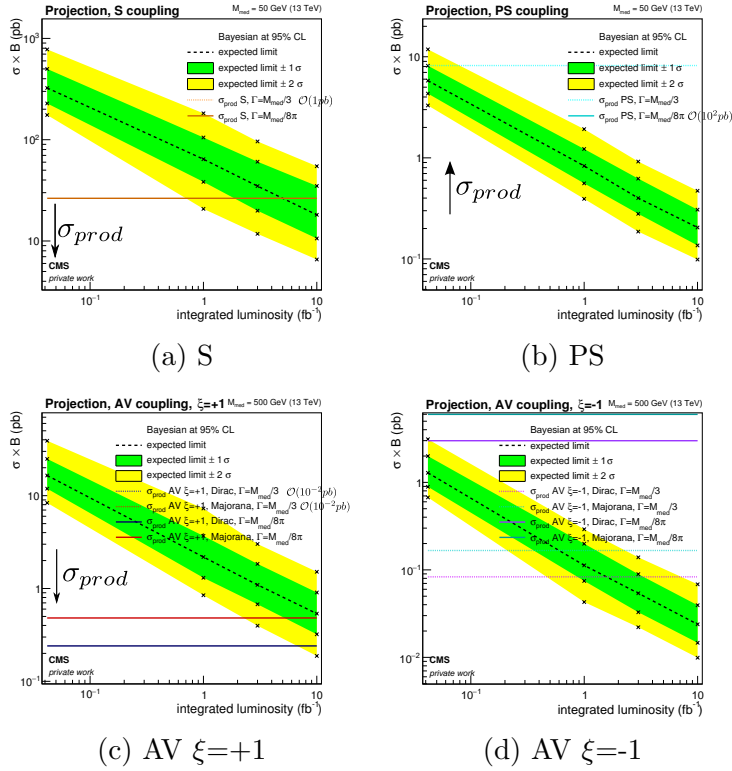Figure 6.13: Projected expected limits of all models for an integrated luminosity of 1 fb^{-1}.
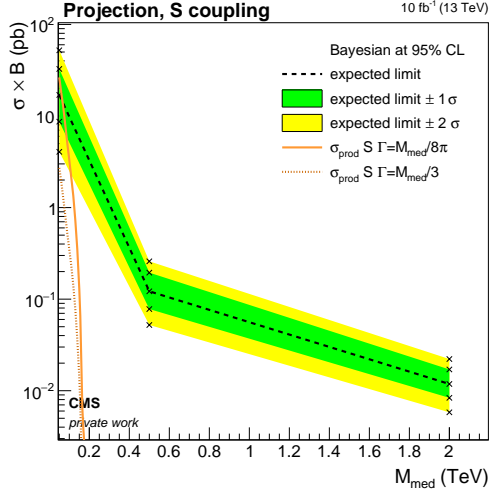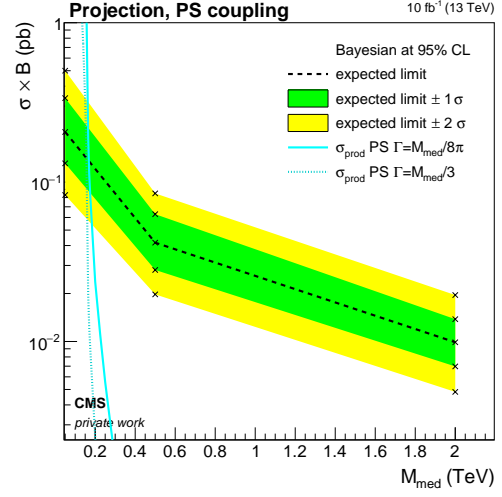

Figure 6.14: Projected expected limits for the AV models at the mass point M$_{med}$=500 GeV and for the (P)S models at the mass point M$_{med}$=50 GeV as a function of the integrated luminosity.

(a) S

(b) PS

(c) AV ξ=1

(d) AV ξ=-1

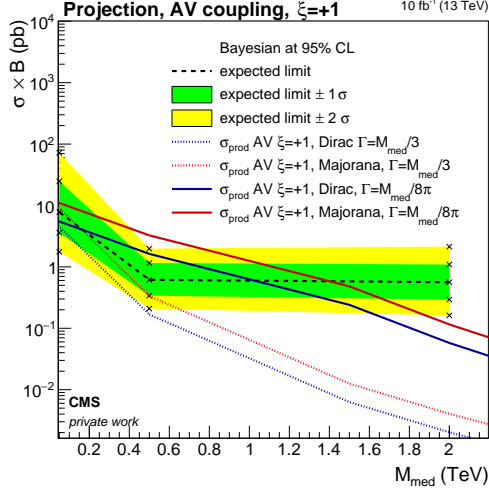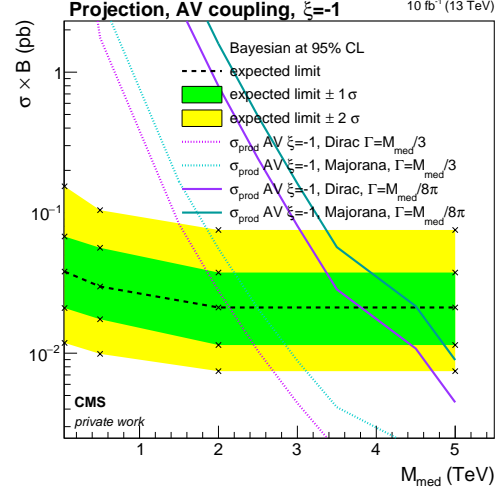Figure 6.15: Projected expected limits of all models for an integrated luminosity of 10 fb^{-1}.

Chapter 7

Discussion of Results

The kinematic selection was optimized for low p_T-triggers and thus a rigorous selection is needed. This can be explained as low p_T triggers reduce the low M_T region only slightly and thus remove only few events with kinematics different from the kinematics of signal events. High p_T triggers, however, reduce the low M_T region significantly and thus a rigorous selection is not needed and might even decrease the sensitivity. As a consequence of these facts it can be expected that high p_T triggers yield the lowest limits when used with a loose selection and low p_T triggers yield the lowest limits when used with a rigorous selection. This can be seen in sections 6.3 and 6.5. It should be noted that compared to the M_T-dependent selections, the static W'_{static} selection is a loose selection.

Low p_T triggers are studied in section 6.3, which indicates that a M_T-dependent kinematic selection indeed is an improvement compared to static kinematic selection for high integrated luminosities. Disregarding specific low M_{med} regions, the W'_{M_T} selection yields the lowest limits in this setup for all models used and are depending on the model an improvement of (1.7 to 38.1)% or a detriment of (3.9 to 41.4)%. In contrast, sections 6.5.1 through 6.5.3 have shown, the W'_{static} selection regularly yields lower limits than the other selections and thus are better suited for searches in both mono-W channels, when applying high p_T triggers. This proves that the optimization of kinematic selection for high p_T triggers have different requirements than an optimization for low p_T triggers.

Using the high p_T trigger and the W'_{static} selection, a range of mediator masses can be excluded for the AV ξ=-1 as well as the PS model, assuming a dark matter mass of m_χ=10 GeV at approximately 41.9pb^{-1}. For the AV ξ=-1 the mediator mass M_{med} has to be bigger than 1880 (2160) GeV for Dirac (Majorana) dark matter particles and a mediator width of $\frac{\Gamma}{M_{med}}$ of $\frac{1}{8\pi}$, while for the PS model the mediator mass M_{med} is restricted to values higher than 155 GeV for the same width. The S and AV ξ=+1 models are not yet sensitive for this luminosity. Assuming an integrated luminosity of 10 fb^{-1} every model is sensitive. The S model is expected to exclude mediators with width $\frac{\Gamma}{M_{med}} = \frac{1}{8\pi}$ and masses $M_{med} < 64$ GeV, while the AV ξ=+1 model is expected to exclude $M_{med} < 1120$ (1500) GeV for Dirac (Majorana) particles and the mediator width $\frac{\Gamma}{M_{med}} = \frac{1}{8\pi}$. In the ξ=-1 case these values increase to $M_{med} < 4090$ (4670) GeV with the same set of assumptions. In the PS model mediator masses $M_{med} < 170$ GeV are expected to be excluded for a width of the mediator of $\frac{\Gamma}{M_{med}} = \frac{1}{8\pi}$.

As a consequence of the different production mechanisms the M_T-dependency of the production cross section of the (P)S models is differs greatly from the production cross section of the AV models. Thus high amounts of integrated luminosity are needed for the (P)S models in

order to gain comparable sensitivity as the AV $\xi=\pm1$ models. The AV ξ=-1 model is sensitive to the biggest phase space of all models studied. As this case might be forbidden [36, 37] possibly limiting the AV model to the ξ=+1 case and that the Majorana approach for dark matter particles is not widely used, further limiting the phase space of comparable results.

In section 6.8 the asymptotic approach is compared to the Bayesian approach. The used (P)S and AV models, did not suffer under the assumption of the asymptotic approach and was in good agreement with the Bayesian approach, which is considered to be a more accurate approach. Because of the asymptotic approach differing between (3 to 15.1)% depending on which model is used, the asymptotic approach should only be used for checks or to roughly estimate the sensitivity of a given process and in depth anaylses should use the Bayesian approach.

Chapter 8

Summary and Outlook

A sensitivity study of the (P)S models has been performed and compared to the AV $\xi=\pm1$ models. It has been found that the CMS detector is already sensitive to the AV $\xi=-1$ and PS models with an integrated luminosity of $\mathcal{L}_{int}=41.9$ pb^{-1} and the range of mediator masses M$_{\mathrm{med}}$, to which the experiment is sensitive, will increase with respect to the integrated luminosity. Sensitivity to the S and AV $\xi=+1$ models developes and also increases with increasing integrated luminosities.

Considering the fact that $\xi\neq+1$ is forbidden for effective field theories and no distinct statement has been made for simplified models yet, the $\xi=+1$ case might be the only allowed case for the AV model. As the CMS is not yet sensitive to this case of the AV model, the PS models might pose as a alternative, that is sensitive even for small integrated luminosities.

Owing to the fact that this channel was proposed in CMS to ensure a complete scan of processes and the sensitivity is now estimated, a follow-up analysis utilizing the full dataset of approximately 2.19 fb^{-1} and aiming to find an excess in data or set limits, assuming no such excess has been found, should be performed. This analysis will be able to utilize the advancements in detector understanding in general and specifically in E_T^{miss}. Possible parameters of interest for this analysis are the mediator width Γ, the coupling of the mediator to the SM g$_{SM}$ and dark matter g$_{DM}$ as well as the dark matter mass m$_\chi$ and the mediator mass M$_{\mathrm{med}}$.

It has been found that by optimizing the kinematic selection an improvement of approximately 38.1% can be achieved when used in conjunction with the trigger it was optimized for. However, it is not an improvement but a detriment to cross section limits when used with other triggers. Thus it may be considered to optimize the kinematic selection for high p$_T$ triggers, assuming these are used.

Bibliography

[1] D. J. Griffiths, *Introduction to elementary particles; 2nd rev. version.* Physics textbook. Wiley, New York, NY, 2008. ISBN: 9783527406012.

[2] C. Wiebusch *et al.*, "Physik Vb: Elementarteilchen und Astrophysik", *lecture notes* (March, 2015) .

[3] P. W. Higgs, "Broken symmetries and the masses of gauge bosons", *Phys. Rev. Lett.* **13** (Oct, 1964) 508–509.

[4] F. Englert and R. Brout, "Broken symmetry and the mass of gauge vector mesons", *Phys. Rev. Lett.* **13** (Aug, 1964) 321–323.

[5] **LHCb** Collaboration, "Observation of J/Ψp Resonances Consistent with Pentaquark States in $\Lambda_b^0 \to$ J/ΨK$^-$p Decays", *Phys. Rev. Lett.* **115** (2015) 072001, `arXiv:1507.03414 [hep-ex]`.

[6] Particle Data Group, "Review of Particle Physics", *Chin. Phys.* **C38** (2014) 090001.

[7] E. Corbelli and P. Salucci, "The Extended Rotation Curve and the Dark Matter Halo of M33", *Mon. Not. Roy. Astron. Soc.* **311** (2000) 441–447, `arXiv:astro-ph/9909252 [astro-ph]`.

[8] M. Milgrom, "MOND theory", *Can. J. Phys.* **93** no. 2, (2015) 107–118, `arXiv:1404.7661 [astro-ph.CO]`.

[9] G. Bertone, *Particle Dark Matter: Observations, Models and Searches.* Cambridge University Press, 2010.

[10] **WMAP** Collaboration, "Nine-year Wilkinson Microwave Anisotropy Probe (WMAP) Observations: Final Maps and Results", `arXiv:1212.5225 [astro-ph]`.

[11] **Planck** Collaboration, "Planck 2015 results. I. Overview of products and scientific results", `arXiv:1502.01582 [astro-ph.CO]`.

[12] M. Trodden and S. M. Carroll, "TASI lectures: Introduction to cosmology", in *Progress in string theory. Proceedings, Summer School, TASI 2003, Boulder, USA, June 2-27, 2003*, pp. 703–793. 2004. `arXiv:astro-ph/0401547 [astro-ph]`.

[13] N. Straumann, "Weak and strong lensing statistics", `arXiv:astro-ph/0108255 [astro-ph]`. [Space Sci. Rev.100,29(2002)].

[14] H. Hoekstra, H. Yee, and M. Gladders, "Current status of weak gravitational lensing", *New Astron. Rev.* **46** (2002) 767–781, arXiv:astro-ph/0205205 [astro-ph].

[15] J.-P. Kneib, "Gravitational lensing and cluster of galaxies", arXiv:astro-ph/0009385 [astro-ph].

[16] M. Bartelmann, "Strong and weak lensing by galaxy clusters", *ASP Conf. Ser.* **301** (2003) 255, arXiv:astro-ph/0207032 [astro-ph].

[17] D. J. Bacon and A. N. Taylor, "Mapping the 3-d dark matter potential with weak shear", *Mon. Not. Roy. Astron. Soc.* **344** (2003) 1307, arXiv:astro-ph/0212266 [astro-ph].

[18] **XENON100** Collaboration, "Dark Matter Results from 225 Live Days of XENON100 Data", *Phys. Rev. Lett.* **109** no. 18, (Nov., 2012) 181301, arXiv:1207.5988 [astro-ph.CO].

[19] **LUX** Collaboration, "First results from the LUX dark matter experiment at the Sanford Underground Research Facility", *Phys. Rev. Lett.* **112** (2014) 091303, arXiv:1310.8214 [astro-ph.CO].

[20] **IceCube** Collaboration, "Search for Dark Matter Annihilation in the Galactic Center with IceCube-79", arXiv:1505.07259 [astro-ph.HE].

[21] **AMS** Collaboration, "High Statistics Measurement of the Positron Fraction in Primary Cosmic Rays of 0.5–500 GeV with the Alpha Magnetic Spectrometer on the International Space Station", *Phys. Rev. Lett.* **113** (2014) 121101.

[22] **AMS** Collaboration, "Electron and Positron Fluxes in Primary Cosmic Rays Measured with the Alpha Magnetic Spectrometer on the International Space Station", *Phys. Rev. Lett.* **113** (2014) 121102.

[23] M. Taoso, G. Bertone, and A. Masiero, "Dark Matter Candidates: A Ten-Point Test", *JCAP* **0803** (2008) 022, arXiv:0711.4996 [astro-ph].

[24] A. Coc, J.-P. Uzan, and E. Vangioni, "Standard big bang nucleosynthesis and primordial CNO Abundances after Planck", *JCAP* **1410** (2014) 050, arXiv:1403.6694 [astro-ph.CO].

[25] S. Ando and K. Ishiwata, "Constraints on decaying dark matter from the extragalactic gamma-ray background", *JCAP* **1505** no. 05, (2015) 024, arXiv:1502.02007 [astro-ph.CO].

[26] D. Harvey, R. Massey, T. Kitching, A. Taylor, and E. Tittley, "The non-gravitational interactions of dark matter in colliding galaxy clusters", *Science* **347** (2015) 1462–1465, arXiv:1503.07675 [astro-ph.CO].

[27] **CMS** Collaboration, "Search for physics beyond the standard model in final states with a lepton and missing transverse energy in proton-proton collisions at sqrt(s) = 8 TeV", *Phys. Rev.* **D91** no. 9, (2015) 092005, arXiv:1408.2745 [hep-ex].

[28] **CMS** Collaboration, "Observation of a new boson at a mass of 125 GeV with the CMS experiment at the LHC", *Phys. Lett.* **B716** (2012) 30–61, `arXiv:1207.7235 [hep-ex]`.

[29] **ATLAS** Collaboration, "Observation of a new particle in the search for the Standard Model Higgs boson with the ATLAS detector at the LHC", *Phys. Lett.* **B716** (2012) 1–29, `arXiv:1207.7214 [hep-ex]`.

[30] Y. Bai, P. Draper, and J. Shelton, "Measuring the Invisible Higgs Width at the 7 and 8 TeV LHC", *JHEP* **07** (2012) 192, `arXiv:1112.4496 [hep-ph]`.

[31] D. Ghosh, R. Godbole, M. Guchait, K. Mohan, and D. Sengupta, "Looking for an Invisible Higgs Signal at the LHC", *Phys. Lett.* **B725** (2013) 344–351, `arXiv:1211.7015 [hep-ph]`.

[32] **ATLAS** Collaboration, "Search for dark matter in events with a hadronically decaying W or Z boson and missing transverse momentum in pp collisions at sqrts = 8 TeV with the ATLAS detector", *Phys. Rev. Lett.* **112** no. 4, (2014) 041802, `arXiv:1309.4017 [hep-ex]`.

[33] D. Noll, "A Study of Dark Matter Models at $\sqrt{s} = 13$ TeV pp Collisions for Mono-Lepton Searches", Bachelors' thesis, Phys. Inst. IIIA, RWTH Aachen, RWTH Aachen, Juli, 2015.

[34] P. Harris, V. V. Khoze, M. Spannowsky, and C. Williams, "Constraining Dark Sectors at Colliders: Beyond the Effective Theory Approach", *Phys. Rev.* **D91** (2015) 055009, `arXiv:1411.0535 [hep-ph]`.

[35] Y. Bai and T. M. P. Tait, "Searches with Mono-Leptons", *Phys. Lett.* **B723** (2013) 384–387, `arXiv:1208.4361 [hep-ph]`.

[36] N. F. Bell, Y. Cai, J. B. Dent, R. K. Leane, and T. J. Weiler, "Dark matter at the LHC: Effective field theories and gauge invariance", *Phys. Rev.* **D92** no. 5, (2015) 053008, `arXiv:1503.07874 [hep-ph]`.

[37] H. Acaroğlu, " A Study of Simplified Models for Dark Matter Searches in pp Collisions", Bachelors' thesis, Phys. Inst. IIIA, RWTH Aachen, Oct, 2015.

[38] P. Harris *et al.*, "Simplified models mono-v", Feb, 2015. `https://indico.cern.ch/event/373997/session/0/contribution/6/attachments/745154/1022237/PCH_SimplifiedModel_14_02_monoV.pdf`. [Online; accessed 30 November 2015].

[39] D. Choudhury and D. P. Roy, "Signatures of an invisibly decaying Higgs particle at LHC", *Phys. Lett.* **B322** (1994) 368–373, `arXiv:hep-ph/9312347 [hep-ph]`.

[40] M. Spira, "QCD effects in Higgs physics", *Fortsch. Phys.* **46** (1998) 203–284, `arXiv:hep-ph/9705337 [hep-ph]`.

[41] J. R. Ellis, M. K. Gaillard, and D. V. Nanopoulos, "A Phenomenological Profile of the Higgs Boson", *Nucl. Phys.* **B106** (1976) 292.

[42] D. Abercrombie *et al.*, "Dark Matter Benchmark Models for Early LHC Run-2 Searches: Report of the ATLAS/CMS Dark Matter Forum", `arXiv:1507.00966 [hep-ex]`.

[43] **LHCb** Collaboration, "The LHCb Detector at the LHC", *JINST* **3** (2008) S08005.

[44] **ALICE** Collaboration, "The ALICE experiment at the CERN LHC", *JINST* **3** (2008) S08002.

[45] **ATLAS** Collaboration, "The ATLAS Experiment at the CERN Large Hadron Collider", *JINST* **3** (2008) S08003.

[46] **CMS** Collaboration, "The CMS experiment at the CERN LHC", *JINST* **3** (2008) S08004.

[47] T. Sakuma and T. McCauley, "Detector and Event Visualization with SketchUp at the CMS Experiment", *J. Phys. Conf. Ser.* **513** (2014) 022032, `arXiv:1311.4942 [physics.ins-det]`.

[48] S. Bolognesi, Y. Gao, A. V. Gritsan, K. Melnikov, M. Schulze, N. V. Tran, and A. Whitbeck, "On the spin and parity of a single-produced resonance at the LHC", *Phys. Rev.* **D86** (2012) 095031, `arXiv:1208.4018 [hep-ph]`.

[49] Y. Gao, A. V. Gritsan, Z. Guo, K. Melnikov, M. Schulze, and N. V. Tran, "Spin determination of single-produced resonances at hadron colliders", *Phys. Rev.* **D81** (2010) 075022, `arXiv:1001.3396 [hep-ph]`.

[50] I. Anderson *et al.*, "Constraining anomalous HVV interactions at proton and lepton colliders", *Phys. Rev.* **D89** no. 3, (2014) 035007, `arXiv:1309.4819 [hep-ph]`.

[51] P. Harris, M. Trovato, K. Hahn, *et al.*, "Simplified models @ 13 tev", April, 2015. `https://indico.cern.ch/event/386106/contribution/0/attachments/770757/1057164/PCH_SMS_07_04.pdf`. [Online; accessed 30 November 2015].

[52] P. Harris, M. Trovato, *et al.*, "Simplified models dark matter(update)", June, 2015. `https://indico.cern.ch/event/400673/contribution/3/attachments/802604/1100018/PCH_SMS_Update_v2.pdf`. [Online; accessed 30 November 2015].

[53] J. Alwall, R. Frederix, S. Frixione, V. Hirschi, F. Maltoni, O. Mattelaer, H. S. Shao, T. Stelzer, P. Torrielli, and M. Zaro, "The automated computation of tree-level and next-to-leading order differential cross sections, and their matching to parton shower simulations", *JHEP* **07** (2014) 079, `arXiv:1405.0301 [hep-ph]`.

[54] T. Sjostrand, S. Mrenna, and P. Z. Skands, "A Brief Introduction to PYTHIA 8.1", *Comput. Phys. Commun.* **178** (2008) 852–867, `arXiv:0710.3820 [hep-ph]`.

[55] **CMS** Collaboration, "Github repository for cmssw." `https://github.com/cms-sw/cmssw`. [Online; accessed 18 December 2015].

[56] S. Frixione, P. Nason, and G. Ridolfi, "A Positive-weight next-to-leading-order Monte Carlo for heavy flavour hadroproduction", *JHEP* **09** (2007) 126, `arXiv:0707.3088 [hep-ph]`.

[57] Aachen 3a CMS working group, "Gitlab repository for tapas", Okt, 2015.
`https://gitlab.cern.ch/aachen-3a/tapas`. [Online; accessed 18 December 2015].

[58] **CMS** Collaboration, "Particle-flow event reconstruction in CMS and performance for jets, taus, and E_T^{miss}", CMS Physics Analysis Summary CMS-PAS-PFT-09-001, 2009. `http://cdsweb.cern.ch/record/1194487`.

[59] **CMS** Collaboration, "Commissioning of the particle-flow event with the first LHC collisions recorded in the CMS detector", CMS Physics Analysis Summary CMS-PAS-PFT-10-001, 2010. `http://cdsweb.cern.ch/record/1247373`.

[60] **CMS** Collaboration, "Determination of jet energy calibration and transverse momentum resolution in CMS", *JINST* **6** (2011) P11002, `arXiv:1107.4277 [physics.ins-det]`.

[61] **CMS** Collaboration, "The CMS Particle Flow Algorithm", in *Proceedings, International Conference on Calorimetry for the High Energy Frontier (CHEF 2013)*, pp. 295–304. 2013. `arXiv:1401.8155 [hep-ex]`.

[62] **CMS** Collaboration, "Performance of electron reconstruction and selection with the CMS detector in proton-proton collisions at $\sqrt{s} = 8\text{TeV}$", *JINST* **10** (2015) P06005, `arXiv:1502.02701 [physics.ins-det]`.

[63] **CMS** Collaboration, "Performance of the CMS missing transverse momentum reconstruction in pp data at sqrts = 8 TeV", *JINST* **10** no. 02, (2015) P02006, `arXiv:1411.0511 [physics.ins-det]`.

[64] **CMS** Collaboration, "Missing transverse energy performance of the CMS detector", *Journal of Instrumentation* **6** (Sept., 2011) 9001, `arXiv:1106.5048 [physics.ins-det]`.

[65] **CMS** Collaboration, "Determination of jet energy calibration and transverse momentum resolution in CMS", *Journal of Instrumentation* **6** (Nov., 2011) 11002, `arXiv:1107.4277 [physics.ins-det]`.

[66] **CMS** Collaboration, "Heep electron id and isolation", Aug, 2014. `https://twiki.cern.ch/twiki/bin/view/CMS/HEEPElectronIdentificationRun2`. [Online; accessed 4 November 2015].

[67] J. Lee, "Update on single electron trigger efficiencies", Oct, 2015. `https://indico.cern.ch/event/455047/contribution/17/attachments/1171290/1691063/151015_EleTriggerStudy_jelee.pdf`. [Online; accessed 19 December 2015].

[68] J. Lee, "Update on single electron trigger efficiencies", Oct, 2015. `https://indico.cern.ch/event/455047/`. [Online; accessed 19 December 2015].

[69] **CMS** Collaboration, "Search for new physics, focused on wprime production, in the single electron/muon plus missing-et final states using pp collision data at $\sqrt{s} = 13$ tev", CMS Analysis Note. `http://cms.cern.ch/iCMS/jsp/openfile.jsp?tp=draft&files=AN2015_226_v7.pdf`.

[70] **CMS** Collaboration, "Search for new physics in final states with a tau and missing transverse energy using pp collisions at $\sqrt{s} = 8$ TeV", CMS Physics Analysis Summary CMS-PAS-EXO-12-011, CERN, Geneva, 2015. `http://cds.cern.ch/record/2002036`.

[71] **CMS** Collaboration, "Search for W' decaying to tau lepton and neutrino in proton-proton collisions at sqrts = 8 TeV", `arXiv:1508.04308 [hep-ex]`.

[72] **CMS Collaboration** Collaboration, "Search for SSM W' production, in the lepton+MET final state at a center-of-mass energy of 13 TeV", Tech. Rep. CMS-PAS-EXO-15-006, CERN, Geneva, 2015. `http://cds.cern.ch/record/2114864`.

[73] **CMS** Collaboration, "Documentation of the roostats-based statistics tools for higgs pag", Nov, 2015. `https://twiki.cern.ch/twiki/bin/viewauth/CMS/SWGuideHiggsAnalysisCombinedLimit`. [Online; accessed 29 November 2015].

[74] **CMS** Collaboration, "Github repository for cms higgs combination toolkit", Aug, 2013. `https://github.com/cms-analysis/HiggsAnalysis-CombinedLimit`. [Online; accessed 29 November 2015].

[75] R. Cousins, "Some comments and discussion points on statistical inference for z"', January, 2016. `https://indico.cern.ch/event/477295/contribution/2/attachments/1209114/1763790/cousins_zprime_stats_11jan2016_final.pdf`. [Online; accessed 15 January 2016].

[76] G. Cowan, K. Cranmer, E. Gross, and O. Vitells, "Asymptotic formulae for likelihood-based tests of new physics", *European Physical Journal C* **71** (Feb., 2011) 1554, `arXiv:1007.1727 [physics.data-an]`.

Acknowledgements

Appendix A

HEEP table

Table A.1: List of requirements of HEEP ID v6.0, HEEP ID is an abbreviation for **H**igh **E**nergy **E**lectron **P**airs **ID**entification [66].

Name	Parameter	Value
Require Ecal Driven		True
Reject Out Of Time		True
EoP	max	10
Barrel values		
$\Delta\eta$	$<$	0.004
$\Delta\phi$	$<$	0.06
hadronic/electromagntic energy	Slope	1
hadronic/electromagntic energy	$<$	0.05
Track Isolation p_T	$<$	5
Had Depth 1	Offset	2
Had Depth 1	Slope	0.03
transverse depth 1 hadronic energy	ρ Slope	0.28
Inner Layer Lost Hits	$<$	1
$|dxy|$	$<$	0.02
R29	$<$	0.9
E^{1x5}/E^{5x5}	$>$	0.83
E^{2x5}/E^{5x5}	$>$	0.94
Endcap values		
$\Delta\eta$	$<$	0.006
$\Delta\phi$	$<$	0.06
hadronic/electromagntic energy	Slope	5
hadronic/electromagntic energy	$<$	0.05
Track Isolation: Track p_T	$<$	5
Had Depth 1	Offset	2.5
Had Depth 1	Slope	0.03
Had Depth 1	ρ Slope	0.28
Inner Layer Lost Hits	$<$	1
$|dxy|$	$<$	0.05
$\sigma_{i\eta i\eta}$	$<$	0.03

Appendix B

Low p$_T$ trigger M$_T$ distributions
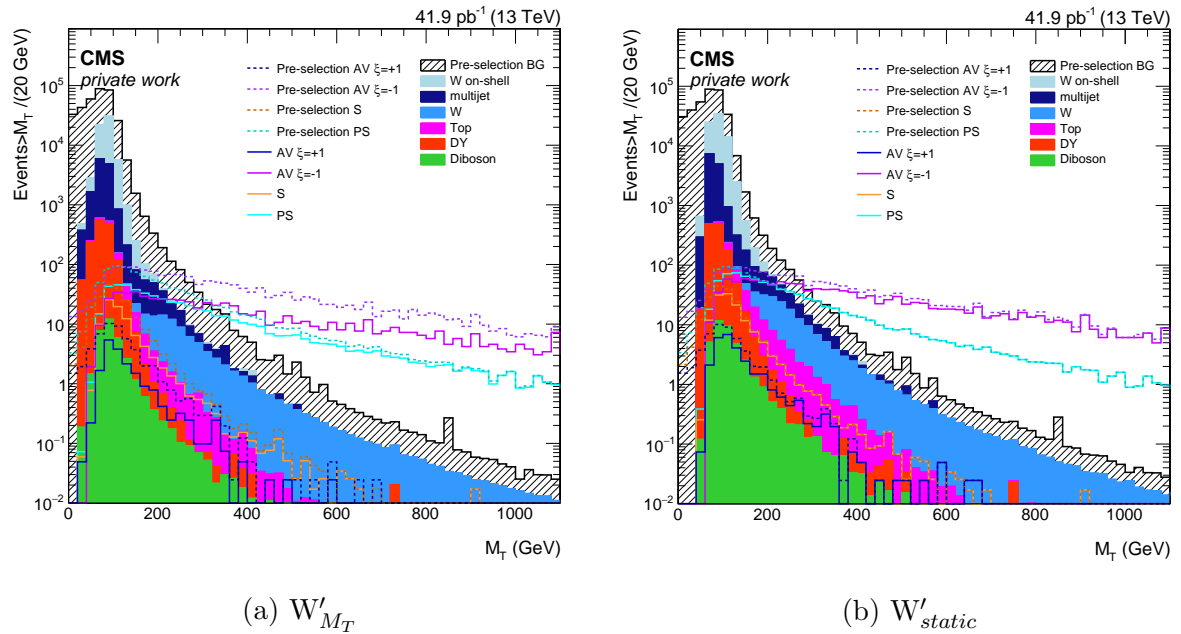

(a) W$'_{M_T}$

(b) W$'_{static}$

Figure B.1: Comparision of M$_T$ distributions: the left distribution uses the W$'_{M_T}$ selection, while the right distribution uses the W$'_{static}$ selection. For both distributions the filled backgrounds are after the respective selection whereas the hatched background is pre-selection. The signals are produced with M$_{med}$=50 GeV.

Appendix C

Completion of selection optimization: tables

Table C.1: Cross section limits in pb for a AV $\xi=+1$ signal are given for each mediator mass point M_{med} and kinematic selection and compared to the W'_{static} selection.

name ╲ M_{med}	50 GeV	500 GeV	2000 GeV
W'_{static} in pb	9.39	0.743	0.690
PS_{90} in pb	13.3	0.643	0.632
comp. to W'_{static}	1.41	0.87	0.92
W'_{M_T} in pb	12.3	0.638	0.612
comp. to W'_{static}	1.31	0.86	0.89

Table C.2: Cross section limits in pb for a AV $\xi=-1$ signal are given for each mediator mass point M_{med} and kinematic selection and compared to the W'_{static} selection.

name ╲ M_{med}	50 GeV	500 GeV	2000 GeV
W'_{static} in pb	0.0455	0.0382	0.0234
PS_{90} in pb	0.0420	0.0359	0.0244
comp. to W'_{static}	0.92	0.94	1.04
W'_{M_T} in pb	0.0418	0.0346	0.0230
comp. to W'_{static}	0.92	0.91	0.98

Table C.3: Cross section limits in pb for a S signal are given for each mediator mass point M_{med} and kinematic selection and compared to the W'_{static} selection.

name ⟍ M_{med}	50 GeV	500 GeV	2000 GeV
W'_{static} in pb	23.9	0.175	0.0166
PS_{90} in pb	25.6	0.136	0.0126
comp. to W'_{static}	1.07	0.78	0.76%
W'_{M_T} in pb	26.6	0.135	0.0124
comp. to W'_{static}	1.11	0.77	0.74

Table C.4: Cross section limits in pb for a PS signal are given for each mediator mass point M_{med} and kinematic selection and compared to the W'_{static} selection.

name ⟍ M_{med}	50 GeV	500 GeV	2000 GeV
W'_{static} in pb	0.369	0.0551	0.0160
PS_{90} in pb	0.228	0.0434	0.0126
comp. to W'_{static}	0.62	0.79	0.79
W'_{M_T} in pb	0.228	0.0430	0.0127
comp. to W'_{static}	0.62	0.78	0.79

Appendix D

M_T tables

D.1 M_T table W'_{M_T} selection

Table D.1: Effects of the W'_{M_T} selection on the SM background, as well as each signal and M_{med} for high p_T triggers. The number of events are given with the statistical uncertainties.

M_{med} name	M_T>500 GeV	M_T>1000 GeV	M_T>1400 GeV
Data	4.0	1.0	0
SM Background	2.87 ± 0.16	0.1954 ± 0.0028	$404.8 \pm 2.2 \cdot 10^{-4}$
PS M_{med}= 50 GeV	94.6 ± 1.5	21.63 ± 0.72	7.88 ± 0.44
S M_{med}= 50 GeV	0.264 ± 0.047	0.0085 ± 0.0085	0 ± 0
AV M_{med}= 50 GeV ξ=-1	306 ± 11	128.0 ± 7.0	61.2 ± 4.8
AV M_{med}= 50 GeV ξ=1	0.025 ± 0.025	0 ± 0	0 ± 0
PS M_{med}= 500 GeV	$301.3 \pm 2.4 \cdot 10^{-7}$	$110.2 \pm 1.4 \cdot 10^{-7}$	$456.1 \pm 9.3 \cdot 10^{-8}$
S M_{med}= 500 GeV	$735.3 \pm 8.2 \cdot 10^{-9}$	$128.7 \pm 3.5 \cdot 10^{-9}$	$34.9 \pm 1.8 \cdot 10^{-9}$
AV M_{med}= 500 GeV ξ=-1	4.10 ± 0.13	1.643 ± 0.081	0.810 ± 0.057
AV M_{med}= 500 GeV ξ=1	0.0301 ± 0.0024	$31.2 \pm 7.8 \cdot 10^{-4}$	$3.9 \pm 2.8 \cdot 10^{-4}$
PS M_{med}= 2000 GeV	$297.8 \pm 1.6 \cdot 10^{-7}$	$196.9 \pm 1.3 \cdot 10^{-7}$	$121.2 \pm 1.0 \cdot 10^{-7}$
S M_{med}= 2000 GeV	$1454.4 \pm 7.3 \cdot 10^{-11}$	$814.6 \pm 5.4 \cdot 10^{-11}$	$392.8 \pm 3.8 \cdot 10^{-11}$
AV M_{med}= 2000 GeV ξ=-1	0.0903 ± 0.0024	0.0451 ± 0.0017	0.0238 ± 0.0012
AV M_{med}= 2000 GeV ξ=1	$102.1 \pm 6.4 \cdot 10^{-5}$	$19.1 \pm 2.7 \cdot 10^{-5}$	$35.4 \pm 9.0 \cdot 10^{-6}$

D.2 M_T table W'_{static} selection

Table D.2: Effects of the W'_{static} selection on the SM background, as well as each signal and M_{med} for high p_T triggers. The number of events are given with the statistical uncertainties.

name \ M_{med}	$M_T > 500$ GeV	$M_T > 1000$ GeV	$M_T > 1400$ GeV
Data	5.0	1.0	0
SM Background	4.89 ± 0.25	0.2462 ± 0.0055	0.0483 ± 0.0027
PS $M_{med} = 50$ GeV	107.8 ± 1.6	21.87 ± 0.73	7.90 ± 0.44
S $M_{med} = 50$ GeV	0.324 ± 0.052	0.0085 ± 0.0085	0 ± 0
AV $M_{med} = 50$ GeV ξ=-1	527 ± 14	174.3 ± 8.2	75.7 ± 5.4
AV $M_{med} = 50$ GeV ξ=1	0.147 ± 0.060	0 ± 0	0 ± 0
PS $M_{med} = 500$ GeV	$431.0 \pm 2.9 \cdot 10^{-7}$	$129.6 \pm 1.6 \cdot 10^{-7}$	$503.6 \pm 9.8 \cdot 10^{-8}$
S $M_{med} = 500$ GeV	$112.6 \pm 1.0 \cdot 10^{-8}$	$152.8 \pm 3.8 \cdot 10^{-9}$	$38.0 \pm 1.9 \cdot 10^{-9}$
AV $M_{med} = 500$ GeV ξ=-1	7.20 ± 0.17	2.256 ± 0.095	0.990 ± 0.063
AV $M_{med} = 500$ GeV ξ=1	0.0437 ± 0.0029	$39.0 \pm 8.7 \cdot 10^{-4}$	$3.9 \pm 2.8 \cdot 10^{-4}$
PS $M_{med} = 2000$ GeV	$397.3 \pm 1.9 \cdot 10^{-7}$	$229.8 \pm 1.4 \cdot 10^{-7}$	$133.9 \pm 1.1 \cdot 10^{-7}$
S $M_{med} = 2000$ GeV	$2013.1 \pm 8.6 \cdot 10^{-11}$	$967.9 \pm 5.9 \cdot 10^{-11}$	$436.5 \pm 4.0 \cdot 10^{-11}$
AV $M_{med} = 2000$ GeV ξ=-1	0.1567 ± 0.0032	0.0609 ± 0.0020	0.0284 ± 0.0013
AV $M_{med} = 2000$ GeV ξ=1	$157.4 \pm 7.9 \cdot 10^{-5}$	$24.6 \pm 3.1 \cdot 10^{-5}$	$4.5 \pm 1.1 \cdot 10^{-5}$

D.3 M_T table PS$_{90}$ selection

Table D.3: Effects of the PS$_{90}$ selection on the SM background, as well as each signal and M_{med} for high p_T triggers. The number of events are given with the statistical uncertainties.

name \ M_{med}	M_T>500 GeV	M_T>1000 GeV	M_T>1400 GeV
Data	4.0	1.0	0
SM Background	3.49 ± 0.20	0.1908 ± 0.0028	$385.5 \pm 2.1 \cdot 10^{-4}$
PS M_{med}= 50 GeV	103.1 ± 1.6	21.78 ± 0.73	7.90 ± 0.44
S M_{med}= 50 GeV	0.290 ± 0.050	0.0085 ± 0.0085	0 ± 0
AV M_{med}= 50 GeV ξ=-1	339 ± 11	125.7 ± 6.9	60.0 ± 4.8
AV M_{med}= 50 GeV ξ=1	0.074 ± 0.042	0 ± 0	0 ± 0
PS M_{med}= 500 GeV	$323.8 \pm 2.5 \cdot 10^{-7}$	$106.8 \pm 1.4 \cdot 10^{-7}$	$433.7 \pm 9.1 \cdot 10^{-8}$
S M_{med}= 500 GeV	$830.4 \pm 8.8 \cdot 10^{-9}$	$124.4 \pm 3.4 \cdot 10^{-9}$	$32.9 \pm 1.7 \cdot 10^{-9}$
AV M_{med}= 500 GeV ξ=-1	4.50 ± 0.13	1.615 ± 0.080	0.773 ± 0.056
AV M_{med}= 500 GeV ξ=1	0.0308 ± 0.0025	$27.3 \pm 7.3 \cdot 10^{-4}$	$3.9 \pm 2.8 \cdot 10^{-4}$
PS M_{med}= 2000 GeV	$304.2 \pm 1.6 \cdot 10^{-7}$	$188.9 \pm 1.3 \cdot 10^{-7}$	$115.2 \pm 1.0 \cdot 10^{-7}$
S M_{med}= 2000 GeV	$1506.9 \pm 7.4 \cdot 10^{-11}$	$779.9 \pm 5.3 \cdot 10^{-11}$	$369.9 \pm 3.7 \cdot 10^{-11}$
AV M_{med}= 2000 GeV ξ=-1	0.0961 ± 0.0025	0.0433 ± 0.0017	0.0228 ± 0.0012
AV M_{med}= 2000 GeV ξ=1	$111.4 \pm 6.6 \cdot 10^{-5}$	$18.6 \pm 2.7 \cdot 10^{-5}$	$27.5 \pm 8.3 \cdot 10^{-6}$

Appendix E

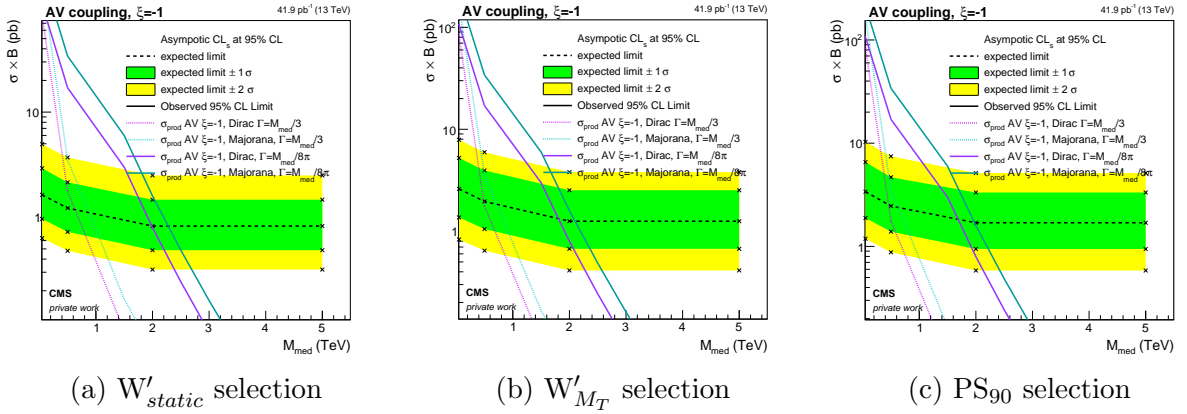# Expected Limit Plots

E.1 Asymptotic expected limits

Figure E.1: Expected limits utilizing the asymptotic approach for the AV ξ=-1 signal and an integrated luminosity of 41.9 pb^{-1}.
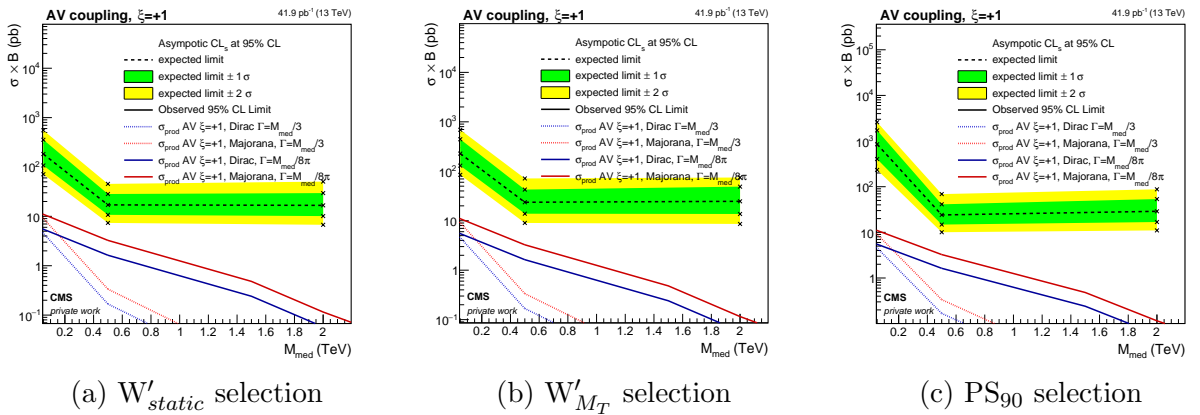

Figure E.2: Expected limits utilizing the asymptotic approach for the AV ξ=+1 signal and an integrated luminosity of 41.9 pb^{-1}.
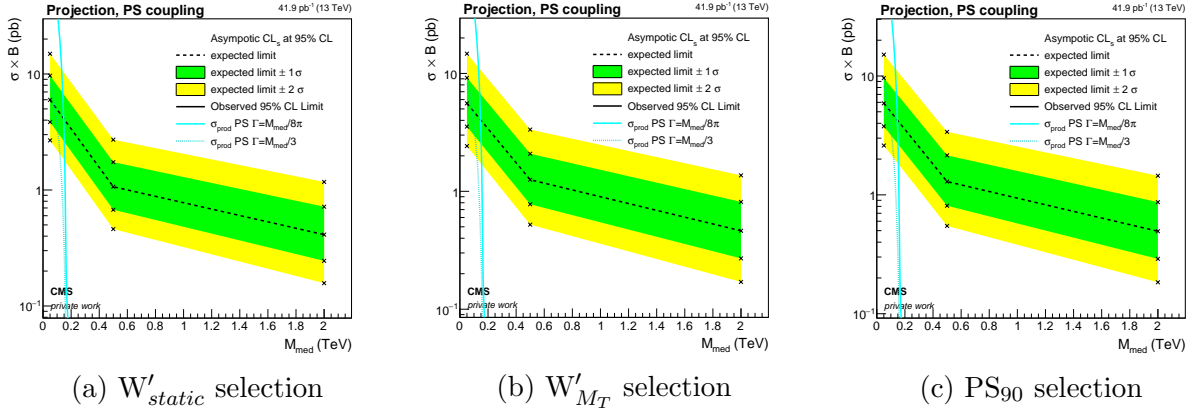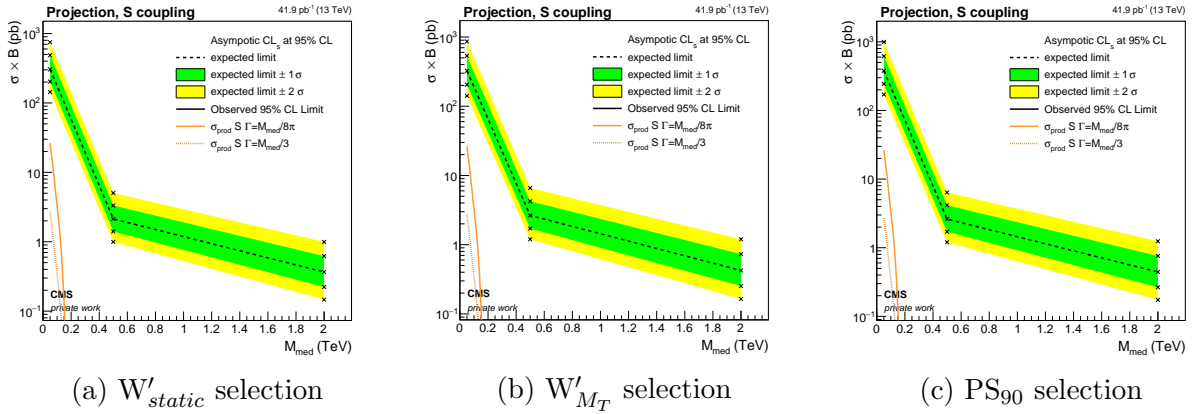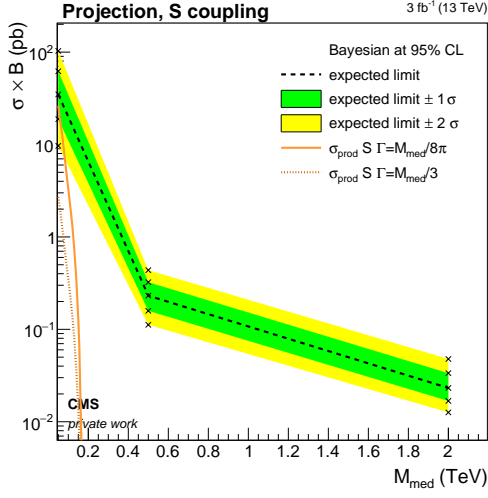
(a) W'_{static} selection   (b) W'_{M_T} selection   (c) PS$_{90}$ selection

Figure E.3: Expected limits utilizing the asymptotic approach for the PS signal and an integrated luminosity of 41.9 pb^{-1}.

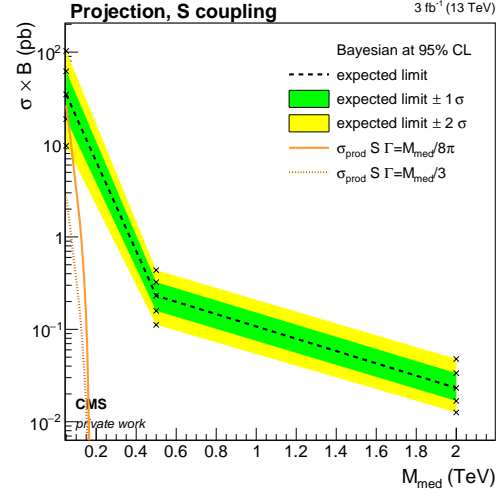(a) W'_{static} selection   (b) W'_{M_T} selection   (c) PS$_{90}$ selection

Figure E.4: Expected limits utilizing the asymptotic approach for the S signal and an integrated luminosity of 41.9 pb^{-1}.
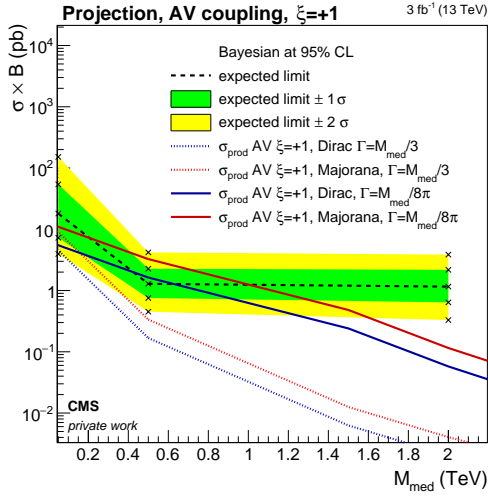
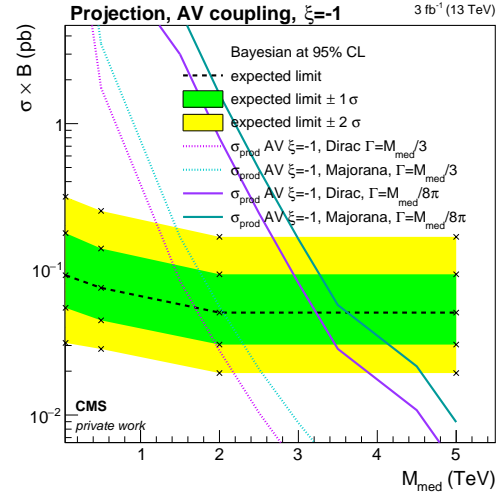# E.2 Projected expected limits for 3 fb^{-1}

(a) expected limits for S

(b) expected limits for PS

(c) expected limits for ξ=+1

(d) expected limits for ξ=-1

Figure E.5: Expected limits of all models for an integrated luminosity of 3 fb^{-1}.

E.3 Projection of expected limits for $M_{med}=50(0)$ GeV

(a) expected limits for S

(b) expected limits for PS

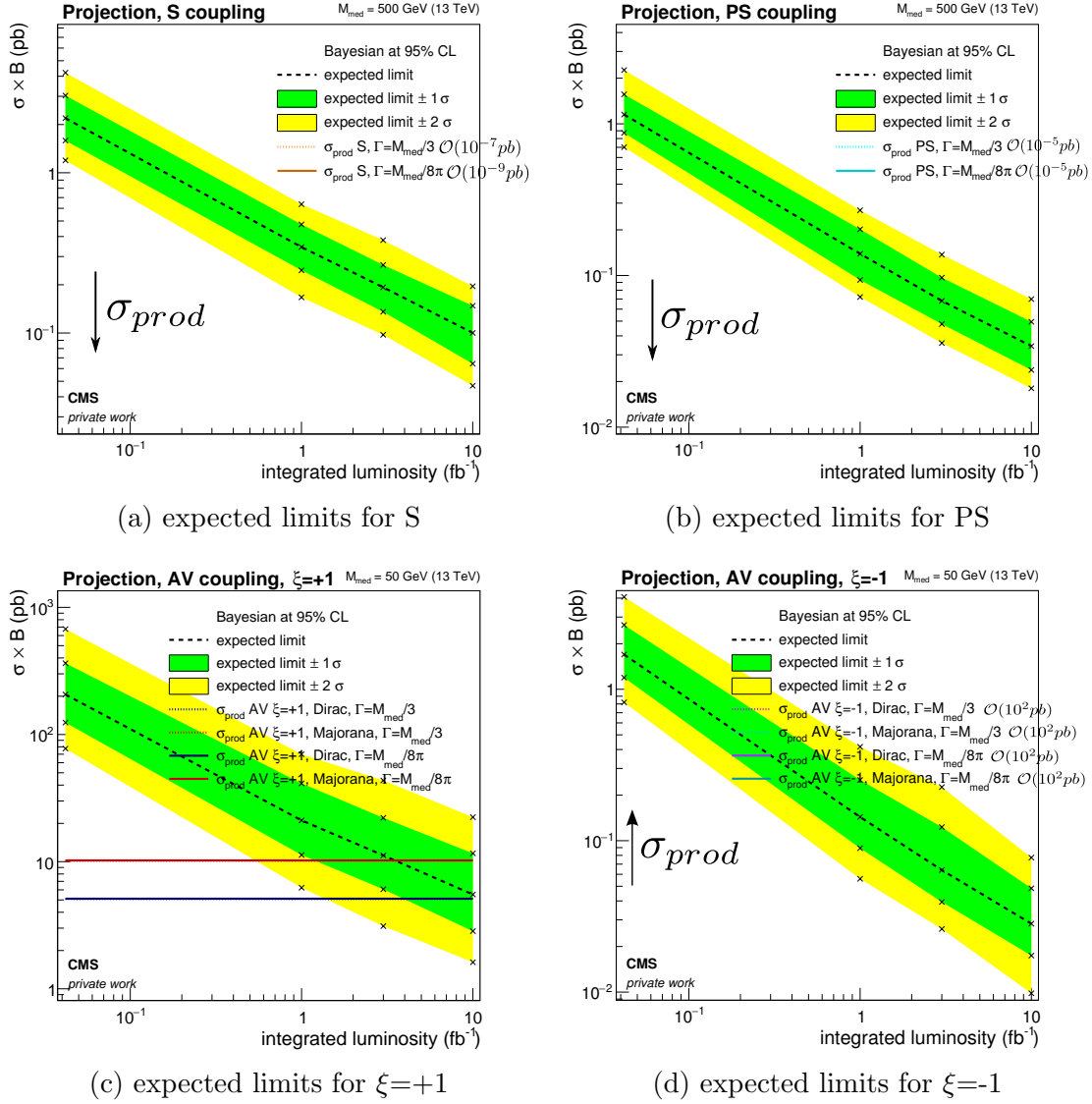(c) expected limits for $\xi=+1$

(d) expected limits for $\xi=-1$

Figure E.6: Expected limits for all models at the mass point $M_{med}=50$ GeV as a function of the integrated luminosity.

E.4 Projection of expected limits for $M_{med}=2000$ GeV

(a) expected limits for S

(b) expected limits for PS

(c) expected limits for ξ=+1
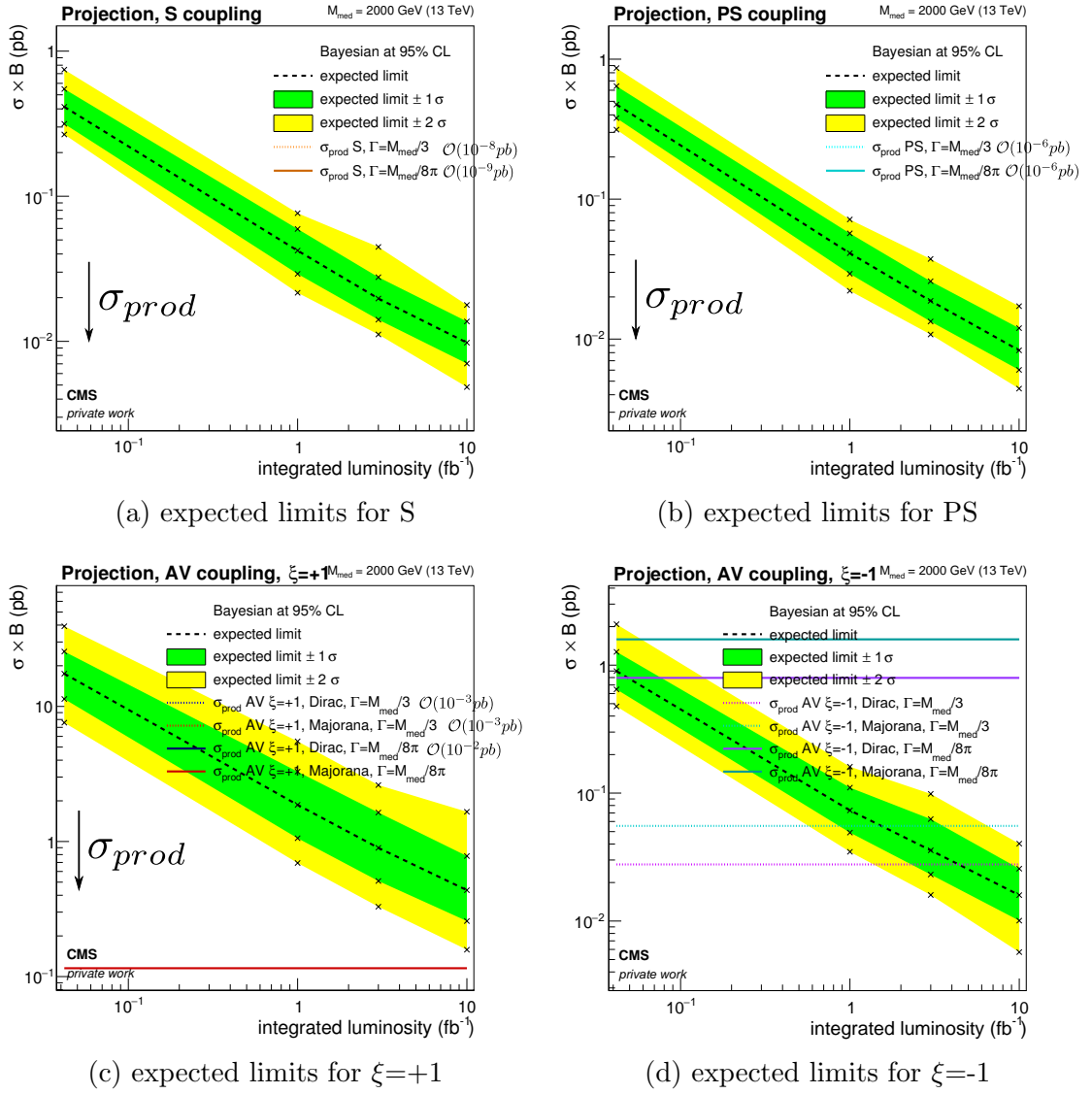
(d) expected limits for ξ=-1

Figure E.7: Expected limits for all models at the mass point $M_{med}=2000$ GeV as a function of the integrated luminosity.